Cell Metabolism

Article

Sweetener aspartame aggravates atherosclerosis through insulin-triggered inflammation

Graphical abstract

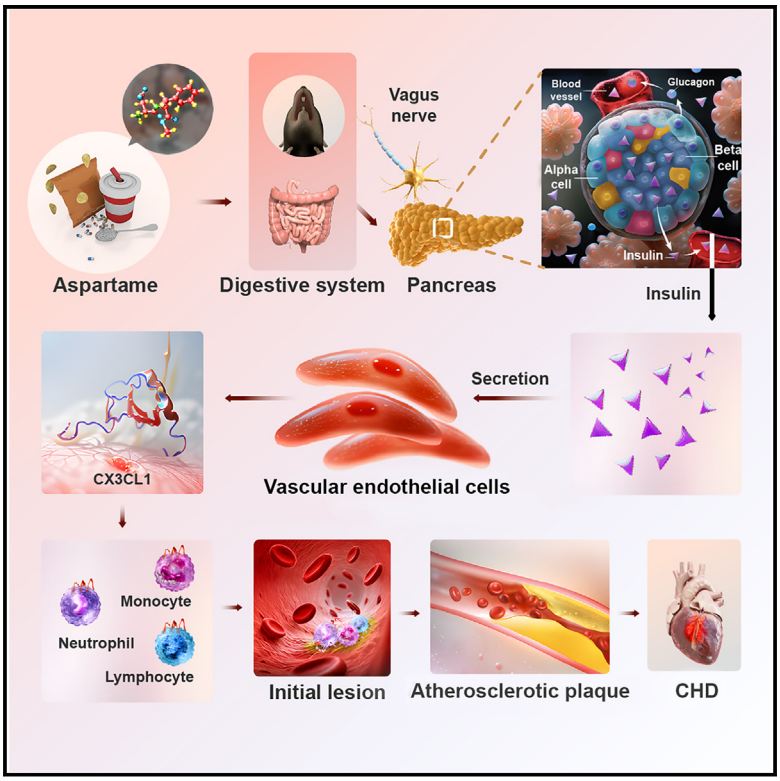

Highlights

- Aspartame increases insulin levels through parasympathetic activation
- An insulin-dependent mechanism of the aspartame-aggravated atherosclerosis
- The CX3CL1-CX3CR1 signaling mediates insulin-induced endothelial inflammation
- A CX3CL1-CX3CR1-dependent mechanism of aspartame-exacerbated atherosclerosis

Authors

Weijie Wu, Wenhai Sui, Sizhe Chen, ..., Yuguo Chen, Cheng Zhang, Yihai Cao

Correspondence

zhangyun@sdu.edu.cn (Y.Z.), chen919085@sdu.edu.cn (Y.C.), zhangc@sdu.edu.cn (C.Z.), yihai.cao@ki.se (Y.C.)

In brief

Wu et al. provide new insights into how aspartame consumption exacerbates atherosclerosis through an insulin-dependent mechanism. Aspartame-triggered high insulin levels upregulate the endothelial membrane-bound inflammatory CX3CL1 and the deletion of the *Cx3cr1* gene completely abrogates the pro-atherosclerotic effect. Our findings suggest a promising therapeutic approach for treating atherosclerosis-associated cerebrocardiovascular diseases.

Wu et al., 2025, Cell Metabolism *37*, 1–14
May 6, 2025
https://doi.org/10.1016/j.cmet.2025.01.006

CellPress

Please cite this article in press as: Wu et al., Sweetener aspartame aggravates atherosclerosis through insulin-triggered inflammation, Cell Metabolism (2025), https://doi.org/10.1016/j.cmet.2025.01.006

Cell Metabolism

CellPress
OPEN ACCESS

Article

Sweetener aspartame aggravates atherosclerosis through insulin-triggered inflammation

Weijie Wu,[1,2] Wenhai Sui,[1,2] Sizhe Chen,[1,2] Ziheng Guo,[3] Xu Jing,[2] Xiaolu Wang,[2] Qun Wang,[2] Xinshuang Yu,[2] Wenjing Xiong,[1,2] Jiansong Ji,[4] Libo Yang,[5] Yuan Zhang,[1] Wenjing Jiang,[1] Guohua Yu,[6] Shuzhen Liu,[6] Wei Tao,[7] Chen Zhao,[8] Yun Zhang,[1,*] Yuguo Chen,[10,*] Cheng Zhang,[1,*] and Yihai Cao[2,9,11,*]

[1]State Key Laboratory for Innovation and Transformation of Luobing Theory, Key Laboratory of Cardiovascular Remodeling and Function Research, Chinese Ministry of Education, Chinese National Health Commission, Chinese Academy of Medical Sciences and Shandong Province, Department of Cardiology, Qilu Hospital of Shandong University, Jinan 250012, China

[2]Department of Microbiology, Tumor and Cell Biology, Hong Kong Centre for Cerebro-cardiovascular Health Engineering, Karolinska Institute, 171 65 Stockholm, Sweden

[3]Department of Pancreatic Surgery, West China Hospital, Sichuan University, Chengdu, China

[4]Key Laboratory of Imaging Diagnosis and Minimally Invasive Intervention Research, The Fifth Affiliated Hospital of Wenzhou Medical University, Affiliated Lishui Hospital of Zhejiang University, The Central Hospital of Zhejiang Lishui, Lishui 323000, China

[5]Department of Endocrinology, The Affiliated Taian City Central Hospital of Qingdao University, Taian City, Shandong Province, China

[6]Clinical Oncology Department, Weifang People's Hospital, Kuiwen, Weifang, China

[7]Center for Nanomedicine and Department of Anesthesiology, Brigham and Women's Hospital, Harvard Medical School, Boston, MA 02115, USA

[8]Eye Institute, Eye and ENT Hospital, Shanghai Medical College, Fudan University, Shanghai, China

[9]Faculty of Medicine, Macau University of Science and Technology, Macau 999078, China

[10]Department Nuclear Medicine, Department of Emergency Medicine, Shandong Provincial Clinical Research Center for Emergency and Critical Care Medicine, Institute of Emergency and Critical Care Medicine of Shandong University, Qilu Hospital of Shandong University, Jinan, China

[11]Lead contact

*Correspondence: zhangyun@sdu.edu.cn (Y.Z.), chen919085@sdu.edu.cn (Y.C.), zhangc@sdu.edu.cn (C.Z.), yihai.cao@ki.se (Y.C.)

https://doi.org/10.1016/j.cmet.2025.01.006

SUMMARY

Consumption of artificial sweeteners (ASWs) in various foods and beverages has been linked to an increased risk of cardiovascular diseases (CVDs). However, molecular mechanisms underlying ASW-associated CVD remain unknown. Here, we show that consumption of 0.15% aspartame (APM) markedly increased insulin secretion in mice and monkeys. Bilateral subdiaphragmatic vagotomy (SDV) obliterated APM-elevated blood insulin levels, demonstrating crucial roles of parasympathetic activation in regulation of insulin secretion. Incessant APM feeding of ApoE$^{-/-}$ mice aggravated atherosclerotic plaque formation and growth via an insulin-dependent mechanism. Implantation of an insulin-slow-release pump in ApoE$^{-/-}$ mice exacerbated atherosclerosis. Whole-genome expression profiling discovered that CX3CL1 chemokine was the most upregulated gene in the insulin-stimulated arterial endothelial cells. Specific deletion of a CX3CL1 receptor, *Cx3cr1* gene, in monocytes/macrophages completely abrogated the APM-exacerbated atherosclerosis. Our findings uncover a novel mechanism of APM-associated atherosclerosis and therapeutic targeting of the endothelial CX3CL1-macrophage CX3CR1 signaling axis provides an approach for treating atherosclerotic CVD.

INTRODUCTION

Artificial sweeteners (ASWs), also known as non-nutritive sweeteners (NNSs), as alternatives to caloric sugar are much appreciated by consumers. Aspartame (APM), as one of the commonly used sweeteners,[1] is approximately 200 times sweeter than sucrose, and its calorific value in added foods and beverages is nearly zero.[2] According to the FDA, maximal recommended daily intake of APM is 40 mg/kg bodyweight in Europe and 50 mg/kg bodyweight in the United States.[2,3] Unfortunately, unintentional APM consumptions by adults and children often exceed those levels recommended by the FDA authorities and are associated to various health complications.[2,4] According to published reports, APM has been associated with various diseases, including obesity, type 2 diabetes mellitus (T2DM), cancer, cardiovascular disease (CVD), allergies, neurological disorders, and behavior disorders.[2,5–12] However, the health impacts of APM consumption, particularly the consequences of its long-term consumption warrant further in-depth investigation.

Accumulating preclinical and clinical studies suggest that ASW consumption is a potential risk factor for CVD by investigating factors, such as hypertension, vascular dysfunction,

Please cite this article in press as: Wu et al., Sweetener aspartame aggravates atherosclerosis through insulin-triggered inflammation, Cell Metabolism (2025), https://doi.org/10.1016/j.cmet.2025.01.006

inflammation, weight gain, and gut microbiota perturbation.[9,13] However, a couple of studies show no adverse effects on bodyweight or glucose homeostasis.[14,15] A recent perspective large cohort study based on 103,388 human participants suggests a potential direct link between higher ASW consumption (especially APM, acesulfame potassium, and sucralose) and high risks of CVD.[5] Thus, most of the published data generally support the participation of ASW consumption in causing CVD.

Insulin resistance and hyperinsulinemia have been suggested as risk factors for CVD in human populations.[16–18] Pancreatic β cells synthesize insulin that gets secreted in response to elevated plasma glucose.[19] In addition to glucose, other nutrients such as free fatty acids (FFAs) and certain amino acids also modulate glucose-induced insulin secretion.[20,21] Parasympathetic activation of the vagus nerve also increases pancreatic insulin secretion.[22] A recent study shows that duodenal neuropod cells transduce luminal stimuli from ASW to the vagus nerve using sweet taste receptors (STRs) and sodium glucose transporters,[23] suggesting that ASW may potentially regulate blood insulin levels. In fact, consumption of ASW in humans results in increased insulin secretion leading to insulin resistance.[24] STRs located within the gastrointestinal track are mainly distributed to enteroendocrine L and K cells and their signaling pathways are similar as those in the oral cavity.[14,25] In response to their ligands, STRs expressed in enteroendocrine L cells secrete glucagon-like peptide-1 (GLP-1) and peptide YY (PYY), which regulate insulin secretion. However, ASW may not be as effective as natural sugar for regulation of insulin secretion.[14,26–28]

Insulin resistance has been causatively linked to development of atherosclerosis,[29] which is the leading cause for CVD-, stroke-, and other artery dysfunction-associated morbidities and mortalities.[30] Several possible mechanisms have been proposed to explain insulin resistance and hyperinsulinemia in atherosclerosis, including dyslipidemia, salt and water retention, and inhibition of fibrinolysis.[31] The other important factor contributing to atherosclerosis is inflammation, which occurs hand-in-hand with emerging lipid accumulation in the arterial wall and participates in initiation, progression, and the thrombotic complications of atherosclerosis.[32] Circulating monocytes interact with activated arterial endothelial cells (AECs) through adhesion molecules and chemokines to promote monocyte migration, activation, and conversion.[33,34] Proinflammatory monocytes/macrophages within intima express scavenger receptors that bind to lipoprotein particles and become foam cells, also named lipid-laden cells, which exhibit the M2-macrophage phenotype.[30,33] Infiltration of inflammatory cells in atherosclerotic plaques (APs) also accelerates plaque growth and instability, two key pathological processes for causing tissue ischemia as seen in myocardial infarction and stroke.[35] The mechanistic link between insulin resistance and hyperinsulinemia remains elusive.

In this study, we provide several novel mechanistic insights into ASW-associated atherosclerosis, including (1) APM increases blood insulin levels in rodents, (2) APM exacerbates the formation and growth of APs in experimental animals, (3) discovery of an insulin-dependent mechanism of APM-triggered atherosclerosis, (4) discovery of the endothelial CX3CL1-monocyte/macrophage CX3CR1 signaling as the causative mechanism for aggravating atherosclerosis, and (5) validation of APM-elevated blood insulin in primates. Our data provide novel mechanistic insights into the ASW-associated atherosclerosis and define several new therapeutic targets for potential treatment of atherosclerosis-associated CVD.

RESULTS

APM exacerbates atherosclerosis in mice

Atherosclerosis is the key pathological process causing CVD,[30] and consumption of ASWs has been linked to high incidences of CVD events.[5] To gain mechanistic insights into the causative link between APM consumption and atherosclerosis, we designed experiments by feeding ApoE$^{-/-}$ mice with various doses of APM in their diet. After a 12-week feeding, significant increases in APs in the aorta were found in the APM-feeding groups relative to the vehicle control group (Figures 1A and 1B). A dose-dependent effect was observed from 0.05% APM to 0.15% APM (w/w). Since sex might play a role in affecting ASW effects,[36] we performed the similar experiments using female mice. APM-induced atherosclerotic effects were observed in both male and female mice (Figures 1 and S1). APM (0.15%) is commonly used in various preclinical mouse models to study its biological effects.[2] We therefore chose this dose for subsequent analysis, although feeding ApoE$^{-/-}$ mice with lower doses of APM also markedly aggravated atherosclerosis.

H&E staining of the aortas corroborated the findings from the gross examination, demonstrating the existence of larger atherosclerotic lesions in the APM group than in the vehicle-fed group (Figures 1C and 1D). Consistent with this, oil-red-O staining showed an abundance of lipids within the APs of the APM-fed group (Figures 1C and 1D). In support of this notion, Sirius-red-positive signals, which define fibrotic caps, were also markedly decreased in the APM group (Figures 1E and 1F). Immunofluorescent analyses demonstrated that plaques in the APM group contained high numbers of inflammatory cells and decreased components of alpha-smooth muscle actin (α-SMA) positive signals, increasing AP instability (Figures 1G and 1H).

To investigate the timeline of APM-induced atherosclerosis, a time-course experiment was performed. At the 4-week early phase of atherosclerosis development, APM consumption increased the number of atherosclerotic lesions and the average plaque size (Figure S2). With prolonged APM feeding, the size of the plaques increased further by the end of weeks 8 and 12 (Figure S2). Histological and immunofluorescence analyses validated the presence of larger APs in the APM-fed group at weeks 4, 8, and 12 (Figure S2). To study the impact of energetic sugars on AP development, we designed another control group by feeding ApoE$^{-/-}$ mice with 15% sucrose. Unlike APM feeding, the addition of 15% sucrose to the diet did not significantly augment AP development by the end of weeks 4 and 8 relative to the vehicle group (Figure S2). However, the AP-promoting effect of sucrose was delayed until the end of week 12 (Figure S2). APM feeding did not significantly alter the bodyweight, fat mass composition, or food intake (Figures S3A–S3C). However, sucrose feeding slightly increased the bodyweight and fat mass composition without affecting food intake (Figures S3A–S3C). Other metabolic parameters, including O_2 consumption, CO_2 production, heat production, total levels of serum cholesterols (CHOLs), serum triglyceride (TG), and circulating high-density lipoprotein (HDL) remained unchanged between the vehicle-, sucrose-, and APM-fed groups,

Please cite this article in press as: Wu et al., Sweetener aspartame aggravates atherosclerosis through insulin-triggered inflammation, Cell Metabolism (2025), https://doi.org/10.1016/j.cmet.2025.01.006

CellPress
OPEN ACCESS

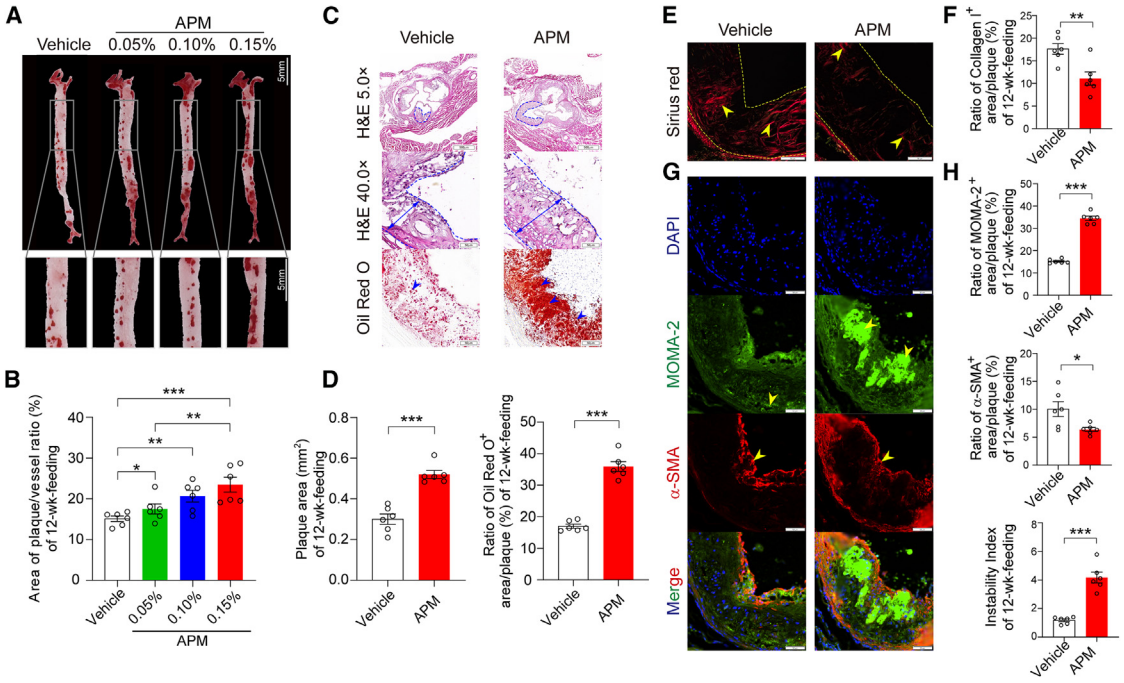

Figure 1. Exacerbation of atherosclerosis by APM supplementation

(A and B) Gross examination and quantification of positive signals of oil-red-O-stained aortas of ApoE$^{-/-}$ mice fed 0.05%, 0.1%, and 0.15% aspartame (APM) in high-fat, high-cholesterol diet at the end of week 12 (n = 6 mice/group). Mice fed a vehicle diet without APM served as a control (n = 6 mice/group). Scale bar, 5 mm.

(C) Histological analysis of aortic roots dissected from mice fed a vehicle diet or 0.15% APM for 12 weeks. Tissue sections were stained with H&E, oil red O. Dashed lines encircle atherosclerotic plaque area, double arrows denote plaque thickness. Blue arrowheads point to oil-red-O-positive signals. Scale bars: upper, 500 μm; middle and lower, 50 μm.

(D) Quantification of plaque areas and oil-red-O-positive signals (n = 6 samples/group).

(E) Sirius red staining of aortas dissected from mice fed a vehicle diet or 0.15% APM for 12 weeks. Dashed lines outline plaques. Yellow arrowheads indicate positive signals. Scale bar, 50 μm.

(F) Quantification of Sirius-red-positive signals (n = 6 samples/group).

(G) Immunofluorescent staining with MOMA-2 and α-SMA counterstained with DAPI. Yellow arrowheads indicate positive signals. Scale bar, 50 μm.

(H) Quantification of MOMA-2- and α-SMA-positive signals (n = 6 samples/group). Plaque instability index (n = 6 samples/group).

Data are presented as mean ± SEM. APM, aspartame; MOMA-2, monocyte and macrophage; α-SMA, alpha-smooth muscle actin.

(B) One-way ANOVA. (D, F, and H) Independent-samples t test. *p < 0.05; **p < 0.01; ***p < 0.001.

except for a slight decrease in serum low-density lipoprotein (LDL), which was observed in the sucrose-fed group (Figures S3D and S3E). These data further indicate that APM promotes AP growth and instability in ApoE$^{-/-}$ mice.

APM augments plasma insulin levels and vagus-nerve-dependent insulin regulation

We studied the effects of APM on plasma insulin and circulating glucose levels. To ensure the oral uptake of sufficient amounts of APM by experimental mice, we developed a method by dropping APM in H_2O onto the mouse face, allowing mice to use their front paws to groom their faces, followed by licking the APM-coated paws. This is an effective method for APM uptake because C57BL/6J mice have been shown to strongly prefer APM sweetener.[37] After 10-min feeding with 0.05%, 0.1%, and 0.15% APM, plasma insulin levels significantly increased relative to the vehicle control group at the 30-min time point (Figure 2A). Although there was lack of statistical differences between the 0.1% and 0.15% groups, the 0.15% group showed higher plasma insulin levels than the 0.05% group. Continuous feeding of mice with 0.15% APM for 12 weeks resulted in persistently high serum insulin levels (Figure 2A), suggesting that long-term consumption of APM might lead to insulin resistance. Despite the increases in plasma insulin levels induced by APM, the levels of circulating glucose remained unchanged (Figure S3F). After 12 weeks of non-stop feeding with APM, experimental mice showed significant insulin resistance as detected by the glucose tolerance test (GTT) and insulin tolerance test (ITT) (Figures 2B and 2C). These data show that APM feeding significantly increases circulating insulin levels and prolonged APM intake leads to the development of insulin resistance in ApoE$^{-/-}$ C57BL/6J mice.

Because rodents might respond to APM through mechanisms different from humans and primates, we performed APM feeding experiments in Cynomolgus monkeys. APM was added to drinking water at a final concentration of 0.15%. The monkeys were starved overnight prior to APM feeding. Interestingly, after 10-min feeding with 0.15% APM or 15% sucrose, a temporary spike in insulin levels was detected in both groups at the 30-min time point (Figure 2D). The increased insulin levels

Please cite this article in press as: Wu et al., Sweetener aspartame aggravates atherosclerosis through insulin-triggered inflammation, Cell Metabolism (2025), https://doi.org/10.1016/j.cmet.2025.01.006

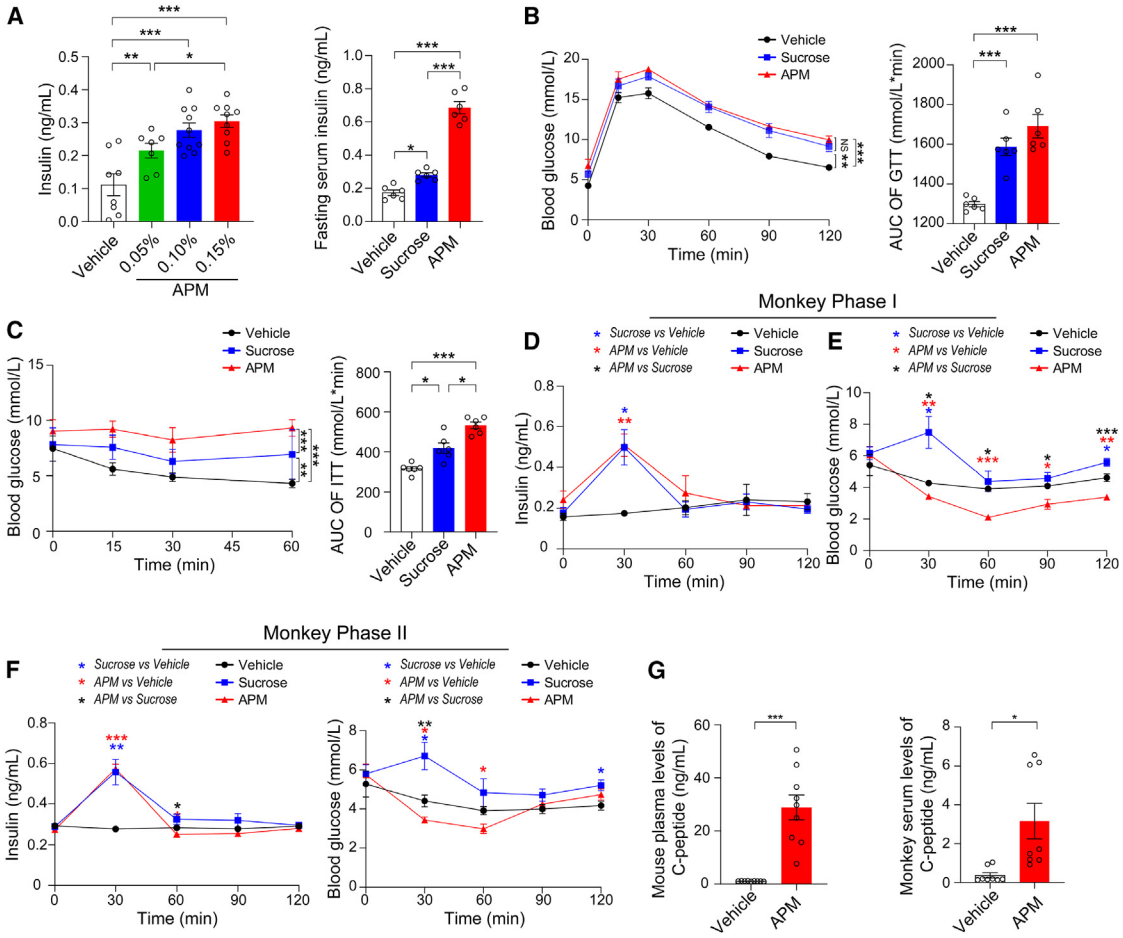

Figure 2. Effects of APM on blood insulin and glucose levels in mice and monkeys

(A) Left: plasma insulin levels after 30-min-feeding with vehicle, 0.05%, 0.1%, and 0.15% aspartame (APM) (n = 7–10 mice/group). Right: serum insulin levels of fasting mice treated with vehicle, 15% sucrose, or 0.15% APM in a high-fat, high-cholesterol diet (HFCD) for 12 weeks (n = 6 mice/group).

(B and C) Glucose and insulin tolerance tests in mice treated with vehicle-, 15% sucrose-, and 0.15% APM-HFCD for 12 weeks, and the data are presented as area under the curve (AUC) in ApoE$^{-/-}$ mice receiving vehicle, 15% sucrose, and 0.15% APM feeding (n = 6 mice/group). (B) Main effect of group: $F = 20.51$, $p < 0.001$; main effect of time: $F = 232.35$, $p < 0.001$; interaction: $F = 0.55$, $p = 0.85$. (C) Main effect of group: $F = 38.71$, $p < 0.001$; main effect of time: $F = 8.42$, $p < 0.01$; interaction: $F = 2.90$, $p = 0.052$.

(D) Cynomolgus monkeys were fed vehicle, 15% sucrose, and 0.15% APM; and serum insulin levels were measured over a period of 2 h (n = 8 monkeys/group). Main effect of group: $F = 2.18$, $p = 0.14$; main effect of time: $F = 12.14$, $p < 0.001$; interaction: $F = 4.64$, $p < 0.001$.

(E) Cynomolgus monkeys were fed vehicle, 15% sucrose, and 0.15% APM; and blood glucose levels were measured over a period of 2 h (n = 8 monkeys/group). Main effect of group: $F = 15.93$, $p < 0.001$; main effect of time: $F = 18.02$, $p < 0.001$; interaction: $F = 4.59$, $p < 0.001$.

(F) The same groups of monkeys were repeatedly fed vehicle, 15% sucrose, and 0.15% APM 3 days after the initial feeding in (D) (n = 8 monkeys/group). Left: main effect of group: $F = 7.04$, $p < 0.01$; main effect of time: $F = 47.25$, $p < 0.001$; interaction: $F = 13.92$, $p < 0.001$. Right: main effect of group: $F = 6.72$, $p < 0.01$; main effect of time: $F = 8.72$, $p < 0.001$; interaction: $F = 3.43$, $p < 0.01$.

(G) C-peptide levels in the plasma of mice and the serum of monkeys treated with vehicle or APM in distilled water, measured 30 min after treatment (n = 8–9 mice or monkeys/group).

Data are presented as mean ± SEM. APM, aspartame; AUC, area under the curve; GTT, glucose tolerance test; ITT, insulin tolerance test.

(A, B right, and C right) One-way ANOVA; (B left, C left, and D–F) repeated measures ANOVA, and (D–F) followed by post hoc Bonferroni analysis; (G) independent-samples t test. *$p < 0.05$; **$p < 0.01$; ***$p < 0.001$. NS, not significant.

returned to basal levels after 60 min (Figure 2D). Noticeably, there was almost no difference in serum insulin levels between the APM and sucrose groups (Figure 2D). Despite nearly identical increases of serum insulin levels in APM- and sucrose-fed groups, polarized serum glucose levels were observed between the two groups (Figure 2E). Although sucrose feeding markedly elevated serum glucose levels, APM feeding produced the opposite effect by significantly mitigating serum glucose levels in these monkeys (Figure 2E). To determine whether the spiking effect of increasing serum insulin levels could be repeated, we performed the same experiment using the same group of monkeys (Figure 2F). Importantly, the insulin-augmenting effects of APM and sucrose were reproduced with repeated feeding. Measurements of circulating levels of C-peptide, a byproduct released after cleavage of proinsulin, showed markedly high levels in the acute APM-fed groups (Figure 2G). Our results

Please cite this article in press as: Wu et al., Sweetener aspartame aggravates atherosclerosis through insulin-triggered inflammation, Cell Metabolism (2025), https://doi.org/10.1016/j.cmet.2025.01.006

CellPress
OPEN ACCESS

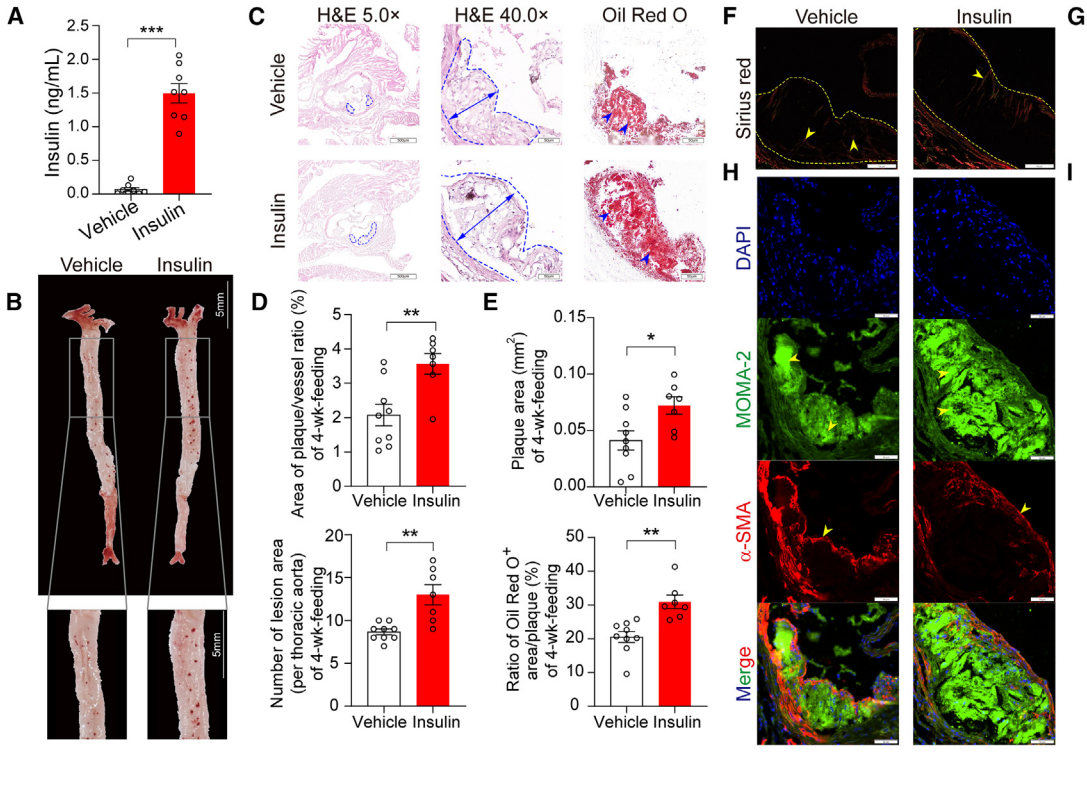

Figure 3. Exacerbation of atherosclerosis by exogenous insulin

(A) Fasting plasma insulin levels in ApoE$^{-/-}$ mice implanted with vehicle- or insulin-releasing mini-osmotic pumps (n = 8 mice/group). Plasma insulin levels were measured 1 week after mini-osmotic pump implantation.

(B) Gross examination of the aorta after oil-red-O staining. Scale bar, 5 mm.

(C) Histological analysis of aorta roots dissected from vehicle- and insulin-releasing pump-implanted mice after 4 weeks. Tissue sections were stained with H&E, oil red O. Dashed lines encircle areas of atherosclerotic plaques, double arrows indicate plaque thickness. Blue arrowheads point to oil-red-O-positive signals. Bars in the left, 500 μm; bars in the middle and right, 50 μm.

(D) Quantification of oil-red-O-positive signals and the number of plaque lesions in thoracic aorta area at the end of week 4 (n = 7–9 mice/group).

(E) Quantification of plaque areas and oil-red-O-positive areas in pump-implanted mice at the end of week 4 (n = 7–9 samples/group).

(F) Sirius red staining of aortas dissected from mice after 4 weeks of treatment with the vehicle- or insulin-releasing pumps. Dashed lines encircle plaques. Yellow arrowheads point to positive signals. Scale bar, 50 μm.

(G) Quantification of Sirius red-positive signals (n = 7–9 samples/group).

(H) Immunofluorescent staining with MOMA-2 and α-SMA counterstained with DAPI. The yellow arrowheads indicate positive signals. Scale bar, 50 μm.

(I) Quantification of MOMA-2- and α-SMA-positive signals and plaque instability index (n = 7–9 samples/group).

Data are presented as mean ± SEM. MOMA-2, monocyte and macrophage; α-SMA, alpha-smooth muscle actin; VEH, vehicle; INS, insulin.

(A, D, E, G, and I) Independent-samples t test. *$p < 0.05$; **$p < 0.01$; ***$p < 0.001$.

demonstrate that APM stimulates insulin secretion in our experimental models. These findings prove that rodents and primates respond to APM feeding by increasing circulating insulin levels and altering insulin sensitivity.

Because APM lacks caloric energy, we hypothesized that it regulated insulin production through a glucose-independent mechanism. It is known that the activation of the vagus nerve augments insulin production.[24] We performed bilateral subdiaphragmatic vagotomy (SDV) in the experimental mice (Figure S3G), followed by APM or vehicle feeding. Notably, SDV completely inhibited the APM-induced insulin production (Figure S3H). Similarly, SDV prevented APM-induced atherosclerosis and AP instability (Figures S3I–S3Q). These results indicate that vagus nerve activation is essential for APM-induced insulin production and atherosclerosis.

Mechanistic insights into insulin-dependent atherosclerosis by gain and loss of function

To further investigate the impact of insulin on atherosclerosis, we employed a gain-of-function approach by subcutaneously implanting a mini-osmotic pump in each animal. The implanted mini-osmotic pump allowed for slow-release of exogenous insulin in the mouse body. To recapitulate the clinical situation, insulin release from the mini-osmotic pump was tightly justified to 1.5 ng/mL (Figure 3A), which was equivalent to a circulating insulin level (25 μIU/mL) in humans above endogenous levels. Similar to APM feeding, this modest increase in circulating insulin levels in ApoE$^{-/-}$ mice markedly aggravated AP formation, growth, and instability by the end of weeks 4 (Figures 3B–3I), 8, and 12 (Figures S4A–S4E). These data demonstrated that the increase in circulating

Please cite this article in press as: Wu et al., Sweetener aspartame aggravates atherosclerosis through insulin-triggered inflammation, Cell Metabolism (2025), https://doi.org/10.1016/j.cmet.2025.01.006

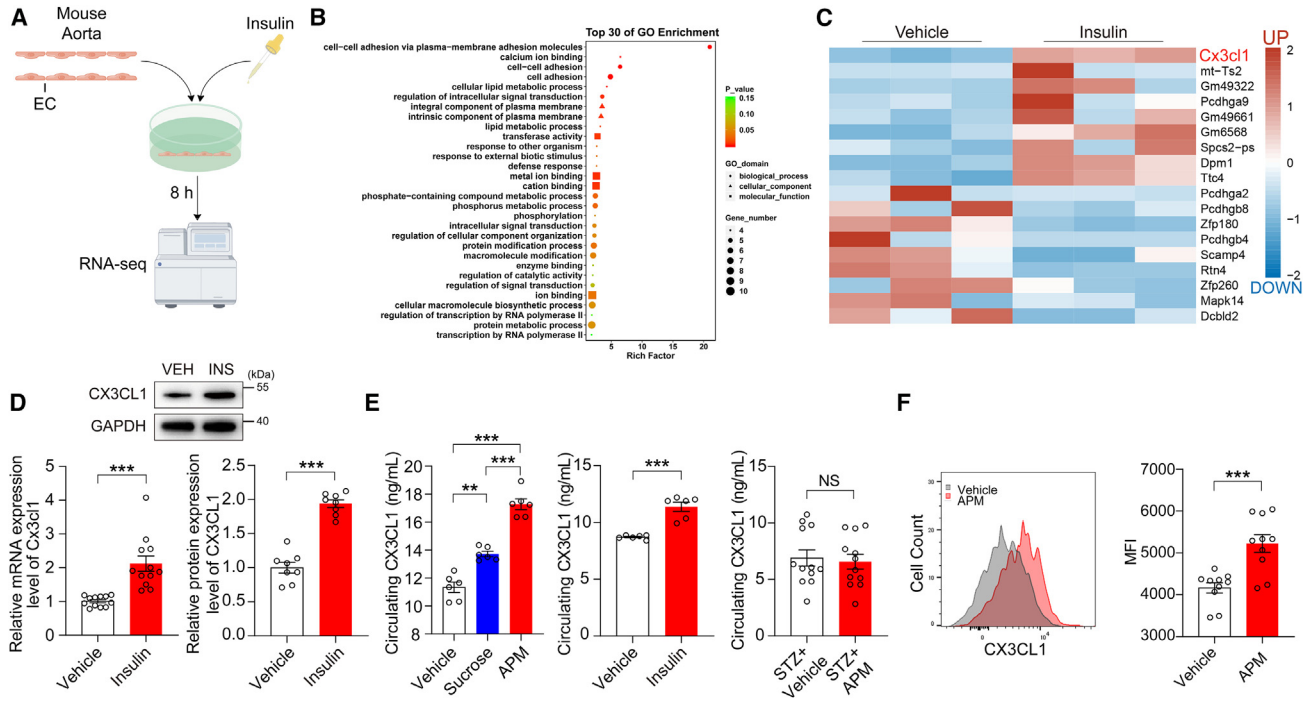

Figure 4. Upregulation of CX3CL1 chemokine by insulin in endothelial cells

(A) Primary aortic endothelial cells (PAECs) were isolated from *wt* C57BL/6J mice and stimulated with 0.8 μg/mL insulin for 8 h. After stimulation, total RNA was extracted for profiling gene expression by RNA-seq.

(B) Gene Ontology (GO) analysis of signaling pathways in the insulin-stimulated PAECs. The top 30 most regulated signaling pathways were profiled.

(C) The top 9 most upregulated and 9 most downregulated genes are presented in heatmap. Cx3cl1 is the most upregulated gene among all genes in the genome after *p* and *q* value corrections.

(D) qPCR quantification of Cx3cl1 mRNA expression levels in vehicle- or insulin-stimulated PAECs ($n = 12$ samples/group). Western blot analysis and quantification of CX3CL1 protein expression levels in vehicle- or insulin-stimulated PAECs ($n = 8$ samples/group).

(E) Circulating CX3CL1 protein levels in vehicle-, insulin-, and STZ-treated mice (12-week treatment; $n = 6$–12 samples/group).

(F) FACS analysis of primary vascular cells from the aortic wall of vehicle- and aspartame (APM)-fed mice ($n = 10$ samples/group).

Data are presented as mean ± SEM. VEH, vehicle; INS, insulin; STZ, streptozotocin; APM, aspartame.

(E left) One-way ANOVA; (D, E middle and right, and F) independent-samples t test. $^{**}p < 0.01$; $^{***}p < 0.001$. NS, not significant.

insulin levels induced by an exogenous delivery approach resembles APM-insulin-signaling-aggravated atherosclerosis in animal models.

In addition to the gain-of-function approach, we performed a loss-of-function experiment using streptozotocin (STZ) to abrogate pancreatic insulin production. Intriguingly, STZ treatment completely neutralized APM-augmented AP formation, growth, and instability (Figures S4F–S4K). These findings prove that insulin upregulation is required for APM-triggered atherosclerosis exacerbation.

Identification of CX3CL1 as an insulin-stimulated artery endothelial chemokine

Endothelial cell (EC) damage and arterial wall dysfunction are the initial triggers of the formation of atherosclerotic lesions. The damaged endothelium in the intima further initiates other pathological processes, including the accumulation of CHOL-rich lipids, inflammation, and smooth muscle cell migration and growth.[30] Thus, identifying the initial trigger of endothelial damage is crucial for understanding the mechanisms of APM-insulin signaling-induced atherosclerosis and subsequent AP progression. For this reason, we isolated primary aorta ECs (PAECs) from wild-type C57BL/6J mice and stimulated these PAECs with insulin *in vitro* (Figure 4A).

After 8 h of insulin stimulation, PAECs were subjected to mRNA-seq analysis to identify the potential signaling molecules involved in insulin-induced atherosclerosis. This unbiased approach allowed us to define the gene expression profiles of the entire PAEC genome. Profiling analysis revealed an extraordinary upregulation of adhesion molecules in the insulin-stimulated PAECs (Figure 4B). Particularly, adhesion molecules that mediate cell-to-cell interactions were abundant (Figure 4B). *Cx3cl1* was the most upregulated mRNA among all genes, after *p* and *q* value corrections (Figure 4C). Interestingly, CX3CL1 is a unique chemokine that exhibits both strong adhesive and chemotactic activities and acts as a chemoattractant gradient from its producing cells.[38] The high expression levels of CX3CL1 mRNA and protein in insulin-stimulated PAECs were corroborated by qPCR and western blotting (Figure 4D; Table S1).

Because CX3CL1 can exist in both soluble and membrane-bound forms, and both are biologically active,[39] we measured circulating and membrane-bound CX3CL1 *in vivo*. Consistent with the RNA sequencing (RNA-seq) data, circulating CX3CL1 protein levels in APM-fed mice were markedly higher relative to

Please cite this article in press as: Wu et al., Sweetener aspartame aggravates atherosclerosis through insulin-triggered inflammation, Cell Metabolism (2025), https://doi.org/10.1016/j.cmet.2025.01.006

vehicle- and sucrose-fed groups (Figure 4E). It should be emphasized that the circulating level of CX3CL1 was significantly higher in the sucrose group than that in the vehicle group (Figure 4E). These results suggest that APM augments CX3CL1 levels via an insulin-dependent mechanism. In line with this hypothesis, exogenously released insulin from an implanted mini-osmotic pump also markedly elevated the circulating CX3CL1 level (Figure 4E). Conversely, STZ treatment completely inhibited APM-induced increase in circulating CX3CL1 levels (Figure 4E). To define the membrane-bound fraction of CX3CL1 molecules, we deployed fluorescence-activated cell sorting (FACS) analysis by sorting the $CD31^{+}/CD45^{-}$ EC population, followed by quantified CX3CL1-positive signals. Expectedly, $CX3CL1^{+}$ signals on the aortic EC surface of the APM group were much stronger than those in the vehicle group (Figure 4F). Taken together, these data demonstrate that APM augments both circulating and EC membrane-bound CX3CL1 *in vivo*.

Chemoattractant and adhesive effects of the CX3CL1-CX3CR1 on monocytes/macrophages

Unlike many other chemokines, CX3CL1 exclusively binds to its receptor CX3CR1, which mediates chemotaxis and adhesion of inflammatory and immune cells.[38,39] CX3CR1 is highly expressed in proinflammatory cells, including monocytes, macrophages, neutrophils, and tissue dendritic cells. Monocytes and macrophages, particularly the M1-subpopulation of macrophages, participate in the initial stages of endothelial layer damage and AP formation. We hypothesized that the CX3CL1-CX3CR1 axis serves as a chemoattractant signaling pathway for macrophage migration, adhesion, and M1 polarization (Figure 5A). To test this hypothesis, we analyzed CX3CR1 expression in RAW264.7 monocytes. Expectedly, high levels of CX3CR1 protein were detected in monocytes (Figure 5B). A specific short hairpin RNA (shRNA) targeting *Cx3cr1* effectively ablated the CX3CR1 protein expression in monocytes (Figure 5B).

To recapitulate the shear stress in article vessels, we developed a cell-to-cell adhesion system named the parallel-plate flow chamber (PPFC) in which monocytes adhered to ECs could be recorded in the presence of shear stress (Figure 5C). A modest number of monocytes adhered to the non-insulin-stimulated PAECs (Figures 5D and 5E). In contrast, insulin-stimulated PAECs markedly enhanced monocyte adhesion by at least 3-fold (Figures 5D and 5E). The insulin-enhanced adhesion of monocytes to PAECs was almost completely inhibited by the delivery of *Cx3cr1*-shRNA into monocytes (Figures 5D and 5E). These data indicate that CX3CL1-CX3CR1 signaling mediates insulin-augmented adhesion interactions between ECs and monocytes. Consistent with these *in vitro* findings, under scanning electron microscopy (SEM), monocyte/macrophage-like inflammatory cells were frequently observed in the luminal layer of aorta endothelium at the early stage (2 weeks) of AP development in the APM group (Figure 5F). Additionally, EM analysis demonstrated early endothelial damage, characterized by a rough surface, polarized tight junctions, and disorganized EC arrangement (Figure 5F). Furthermore, the accumulation of lipid components in the intimal layer of the aorta was detected by transmission electron microscopy (TEM) in APM-fed animals but not in the control group (Figure 5F).

In addition to enhancing monocyte-EC adhesion, activation of CX3CL1-CX3CR1 signaling potently induced monocyte migration in a dose-dependent manner (Figure 5G). The CX3CL1-CX3CR1 signaling was also committed to M0 macrophage-M1 macrophage polarization by expressing high levels of inducible nitric oxide synthase (iNOS) (Figure 5H; Table S1). These M1 macrophages expressed high levels of tumor necrosis factor alpha (TNF-α), interleukin-6 (IL-6), and interleukin-1 beta (IL-1β) (Figure 5H; Table S1), demonstrating the proinflammatory nature of these cells.

Deletion of $Cx3cr1^{M\Phi-/-}$ mitigates proinflammatory myeloid cell populations

To provide conclusive evidence of CX3CL1-CX3CR1 signaling mediating pro-atherosclerotic effect of APM, we employed a genetic loss-of-function approach by specifically deleting *Cx3cr1* gene in monocytes and macrophages. Specific knockout of *Cx3cr1* in C57BL/6J mice was achieved using the lysozyme-driven Cre recombinase and insertion of *LoxP* sites flanking the *Cx3cr1* gene (Figure 6A). This genetic approach efficiently eliminated the *Cx3cr1* gene from macrophages isolated from the abdominal cavity (Figure 6A). This $Cx3cr1^{M\Phi-/-}$ strain was crossed with $ApoE^{-/-}$ mice to create $Cx3cr1^{M\Phi-/-}/ApoE^{-/-}$ double-knockout mice.

We employed an unbiased single-cell RNA-seq (scRNA-seq) approach to define peripheral blood mononuclear cell (PBMC) populations in both control $Cx3cr1^{flox/flox}$ wild-type and $Cx3cr1^{M\Phi-/-}$ mice. Following quality control and doublet deletion, a total number of 106,065 cells were passed through the filters with an average of 1,018 genes per cell. A total number of 54,603 cells with an average of 1,033 genes per cell in the $Cx3cr1^{flox/flox}$ group and 51,462 cells with an average of 1,000 genes per cell in $Cx3cr1^{M\Phi-/-}$ were analyzed using the 10× genomics system (Figure S5A; Table S2). Unsupervised clustering revealed 13 cell clusters after reducing the dimensions with uniform manifold approximation and projection (UMAP) (Figure S5B). According to the dot-plot analysis and classically available cell markers, the 13-cell clusters were further divided into 6 cell populations (Figures 6B, 6C, and S5C; Table S3). The composition of the 6-identified cell populations include 43.1% B cells, 32.3% T cells, 16.0% myeloid cells, 7.0% natural killer (NK) cells, 1.2% red blood cells, and 0.4% basophils (Figure S5D).

Interestingly, the myeloid population was markedly decreased by approximately 2-fold in $Cx3cr1^{M\Phi-/-}$ mice relative to the $Cx3cr1^{flox/flox}$ control mice (Figure 6D). Other cell populations remained largely unchanged except for a slight increase in the B cell population in $Cx3cr1^{M\Phi-/-}$ mice. Based on these findings, we focused our subsequent studies on the myeloid population, which was further classified into 15 subpopulations using dot-plot and UMAP analyses (Figures S5E and S5F). Non-myeloid cells, including B cells, T cells, hematopoietic stem and progenitor cells (HSPCs), platelets, and low-quality cells, were further excluded and the pure myeloid cell population was used for subsequent analyses (Figures 6E and 6F). Within the myeloid population, the monocytes/macrophages, according to the dot-plot and UMAP analyses, were classified into 6 subpopulations (Mono-c1, Mono-c2, Mono-c3, Mono-c4, Macro-c5, and Macro-c6) (Figures 6E and 6F). Notably, the Mono-c1 subpopulation was significantly reduced in $Cx3cr1^{M\Phi-/-}$ mice, whereas Mono-c3 and Macro-c5 subpopulations were increased in the $Cx3cr1^{M\Phi-/-}$ mice (Figure 6G).

Please cite this article in press as: Wu et al., Sweetener aspartame aggravates atherosclerosis through insulin-triggered inflammation, Cell Metabolism (2025), https://doi.org/10.1016/j.cmet.2025.01.006

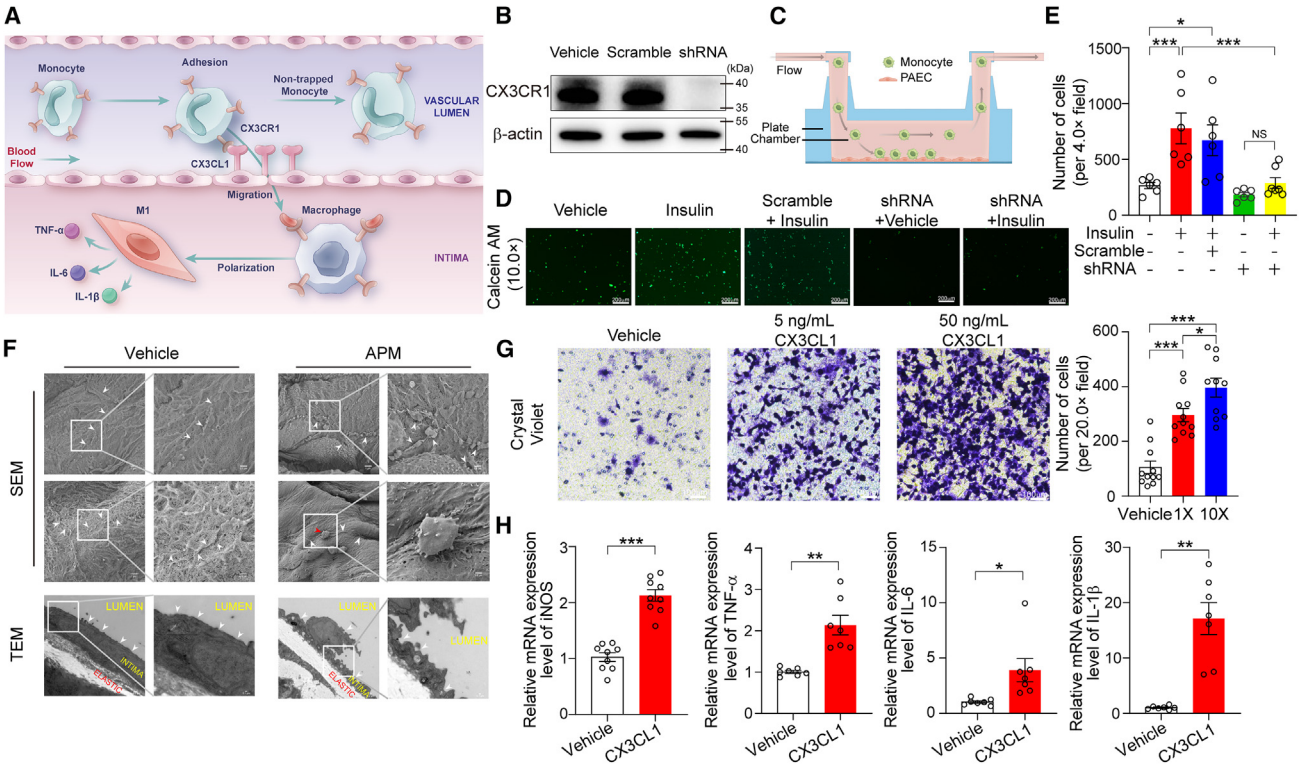

Figure 5. The CX3CL1-CX3CR1 signaling pathway mediates adhesive interactions between endothelial cells and monocytes

(A) Mechanistic diagram illustrating the trapping of mobile CX3CR1^{+} monocytes in the blood stream of arterial vessels by CX3CL1-expressing endothelial cells. Aspartame (APM)-augmented high circulating insulin levels upregulate CX3CL1 expression in endothelial cells. CX3CL1 molecules remain membrane bound on the endothelial cell surface and adhere passing-by CX3CR1^{+} monocytes in the blood stream. The CX3CR1^{+} monocytes adhered to endothelial cells transmigrate through the arterial vessel wall to become intimal resident macrophages, which can undergo phenotypic transitions in response to various cytokine stimuli and secrete a range of cytokines.

(B) Western blot analysis of CX3CR1 expression levels in RAW 264.7 cells after shRNA knockdown using a lentiviral vector. A scrambled shRNA probe was used as a control. β-actin was used to normalize the loading level of each lane.

(C) Illustrative diagram showing the device chamber system to investigate adhesive interactions between endothelial cells and moving monocytes under shear stress. Monocytes were labeled with calcein AM, which is converted into intracellular fluorescence-positive calcein by hydrolysis. Primary aorta endothelial cells (PAECs) were seeded on the bottom of the chamber, and monocytes were added to the flowing medium. Adhered monocytes were analyzed by a fluorescence microscope.

(D) Micrographs of calcein^{+} monocytes adhered to the monolayers of PAECs. Scale bar, 200 μm.

(E) Quantification of adhesive monocytes to the endothelial cell layer under low-power (4×) fields (n = 6–7 random fields/group).

(F) Scanning electron microscopy (SEM) and transmission electron microscopy (TEM) analyses of aortas from vehicle- and APM-fed mice. SEM images show the luminal side of aortas in vehicle and APM groups. White arrowheads mark endothelial tight junctions. The red arrowhead points to the adhered immune cells. TEM images show the smoothness of endothelium and the intima of vessel walls. Arrowheads indicate endothelial layer, and stars mark lipid droplets. Scale bar, 1 μm in the left of SEM. Scale bar, 0.5 μm in the right of SEM. Scale bar, 0.2 μm in the left of TEM. Scale bar, 0.1 μm in the right of TEM.

(G) Analysis of monocyte migration using the Boyden chambers in response to vehicle and soluble CX3CL1 stimulation. Migrated cells were photographed and quantified (n = 10–11 random fields/group) using a light microscope. Scale bar, 100 μm.

(H) Alterations in mRNA expression levels of inducible nitric oxide synthase (iNOS), TNF-α, IL-6, and IL-1β in vehicle- and CX3CL1-stimulated primary mouse macrophages (n = 7–9 samples/group).

Data are presented as mean ± SEM. iNOS, inducible nitric oxide synthase; TNF-α, tumor necrosis factor alpha; IL-6, interleukin-6; IL-1β, interleukin-1 beta; APM, aspartame.

(E and G) One-way ANOVA; (H) independent-samples t test. *p < 0.05; **p < 0.01; ***p < 0.001. NS, not significant.

To simulate the monocyte/macrophage differentiation trajectory, pseudotime analysis was applied to the monocytes/macrophage lineages, which suggested the differentiation trajectory order: Mono-c3 to Mono-c2 to Mono-c1 to Mono-c4. Mono-c3 and Mono-c1/c4 exhibited polarization (Figure 7A), suggesting phenotypic and functional differences. In Cx3cr1$^{M\Phi-/-}$ mice, the Mono-c1 decrease and Mono-c3 increase indicated that the CX3CL1-CX3CR1 signaling axis significantly affected monocyte differentiation. Together, our genetic loss-of-function data demonstrate that the CX3CL1-CX3CR1 signaling axis plays a pivotal role in modulating the composition and functions of myelocytic cells.

Genetic loss of function of Cx3cr1$^{M\Phi-/-}$ neutralizes APM-exacerbated atherosclerosis

We next investigated the possible functions of various monocytes/macrophages in Cx3cr1$^{flox/flox}$ and Cx3cr1$^{M\Phi-/-}$ mice. Gene Ontology (GO) enrichment scores showed that

Please cite this article in press as: Wu et al., Sweetener aspartame aggravates atherosclerosis through insulin-triggered inflammation, Cell Metabolism (2025), https://doi.org/10.1016/j.cmet.2025.01.006

CellPress
OPEN ACCESS

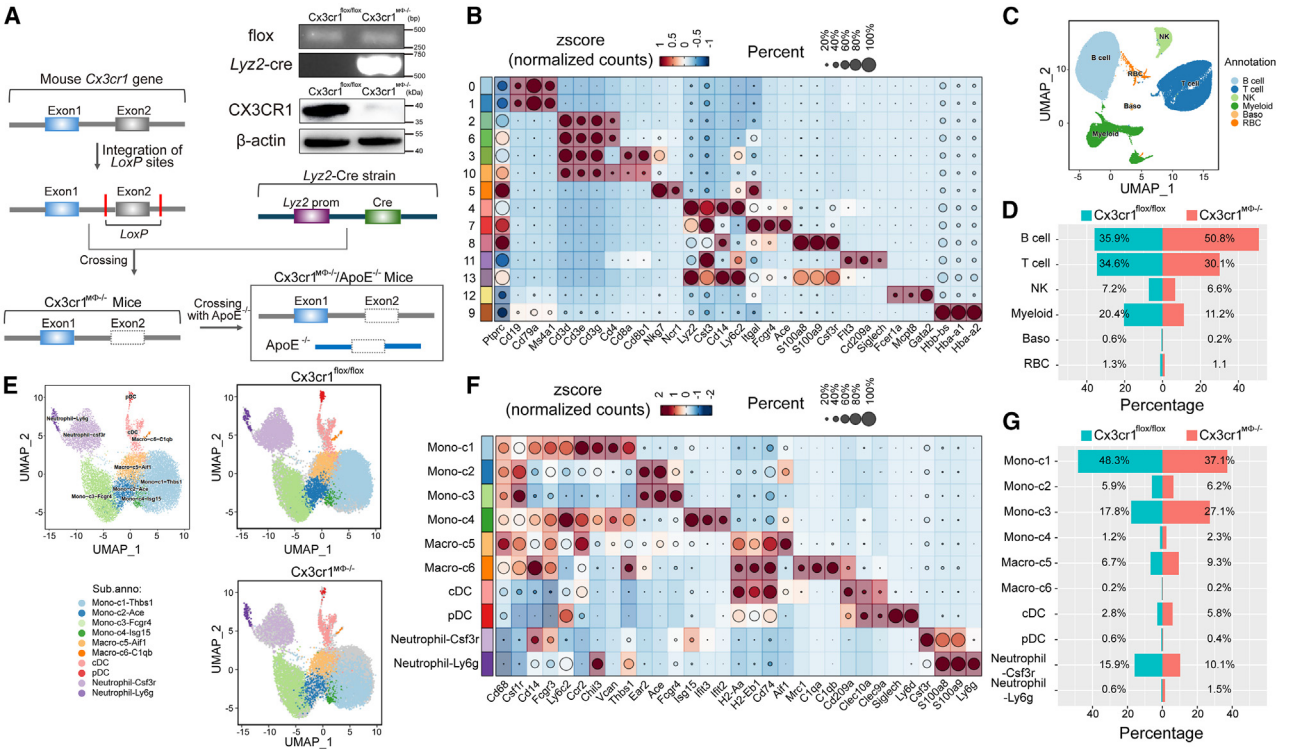

Figure 6. scRNA-seq of PBMCs in Cx3cr1$^{M\Phi-/-}$ mice

(A) Schematic diagram illustrates genetic deletion of *Cx3cr1* gene in monocytes and macrophages. A *LoxP* site was inserted flanking the 5′ end and 3′ end of mouse *Cx3cr1* gene, generating the Cx3cr1$^{flox/flox}$ transgenic mouse line. A *Lyz2*-promoter-driven Cre mouse line (*Lyz2*-Cre) was also generated. Crossing Cx3cr1$^{flox/flox}$ mice with *Lyz2*-Cre mice produced the Cx3cr1$^{M\Phi-/-}$ knockout strain that specifically lacked *Cx3cr1* in monocytes and macrophages. The Cx3cr1$^{M\Phi-/-}$ strain was further cross-bred with ApoE$^{-/-}$ mice to generate the Cx3cr1$^{M\Phi-/-}$/ApoE$^{-/-}$ double-knockout strain. Validation of effective deletion of *Cx3cr1* gene was performed using tails isolated from Cx3cr1$^{M\Phi-/-}$/ApoE$^{-/-}$ double-knockout mice. The deficient expression of CX3CR1 protein in primary macrophages isolated from Cx3cr1$^{M\Phi-/-}$/ApoE$^{-/-}$ double-knockout mice was validated by western blot analysis.

(B) A dot plot shows the relative expression of marker genes in various cell populations. The size of each dot represents the expression percentage of selected genes in each cell population (*n* = 3 samples/group).

(C) UMAP clustering of PBMCs were color coded by different clusters (*n* = 3 samples/group).

(D) Percentage distribution of each cell population in Cx3cr1$^{flox/flox}$ and Cx3cr1$^{M\Phi-/-}$ samples (*n* = 3 samples/group).

(E) UMAP clustering of myeloid cell populations (*n* = 3 samples/group).

(F) Dot plot data show relative expression of marker genes in various myeloid subpopulations. The size of each dot represents the expression percentage of selected genes in each cell population (*n* = 3 samples/group).

(G) Percentage distribution of myeloid cell populations in Cx3cr1$^{flox/flox}$ and Cx3cr1$^{M\Phi-/-}$ samples (*n* = 3 samples/group).

cDC, conventional dendritic cell; pDC, plasmacytoid dendritic cell; HSPC, hematopoietic stem and progenitor cell.

Mono-c1, Mono-c4, and Macro-c6 possessed proinflammatory features, whereas Mono-c2, Mono-c3, and Macro-c5 exhibited anti-inflammatory characteristics (Figure 7B). Analysis of differentially expressed genes (DEGs) showed that Mono-c1 entailed pro-inflammation and adhesion, whereas Mono-c3 exhibited anti-inflammatory and anti-atherosclerotic effects (Figures 7C and S5G). Macro-c5 was involved in antigen presentation and anti-atherosclerosis (Figures 7C and S5G). Given the fact that the decrease of the Mono-c1 subpopulation and increases in Mono-c3 and Macro-c5 populations in Cx3cr1$^{M\Phi-/-}$ mice, genetic deletion of *Cx3cr1* in monocytes/macrophages drifted these cells toward an anti-inflammatory population. If so, Cx3cr1$^{M\Phi-/-}$ mice would alleviate atherosclerosis in the ApoE$^{-/-}$ background. We therefore cross-bred Cx3cr1$^{M\Phi-/-}$ mice with ApoE$^{-/-}$ mice to generate the double-knockout strain of Cx3cr1$^{M\Phi-/-}$/ApoE$^{-/-}$ mice (Figure 6A).

The APM-augmented AP formation and growth were completely neutralized in the Cx3cr1$^{M\Phi-/-}$/ApoE$^{-/-}$ double-knockout mice compared with those in vehicle groups (Figure 7D). At the 4-week early stage of AP development, it became obvious that genetic deletion of *Cx3cr1* in macrophages markedly inhibited the initial formation of atherosclerotic lesions (Figure 7E). With time, the anti-atherosclerotic effect in Cx3cr1$^{M\Phi-/-}$/ApoE$^{-/-}$ double-knockout mice further overtly improved at weeks 8 and 12 (Figures 7F and S6). The AP numbers and sizes were indistinguishable in the APM- and vehicle-fed groups at all time points (Figures 7E, 7F, and S6). Reconciling these findings with gross examination, the accelerated AP growth and instability were further corroborated by histological and immunofluorescence analyses (Figures S6 and S7). In summary, these results demonstrate that CX3CL1-CX3CR1 signaling is responsible for mediating APM-triggered AP aggravation through macrophage-EC crosstalk.

Please cite this article in press as: Wu et al., Sweetener aspartame aggravates atherosclerosis through insulin-triggered inflammation, Cell Metabolism (2025), https://doi.org/10.1016/j.cmet.2025.01.006

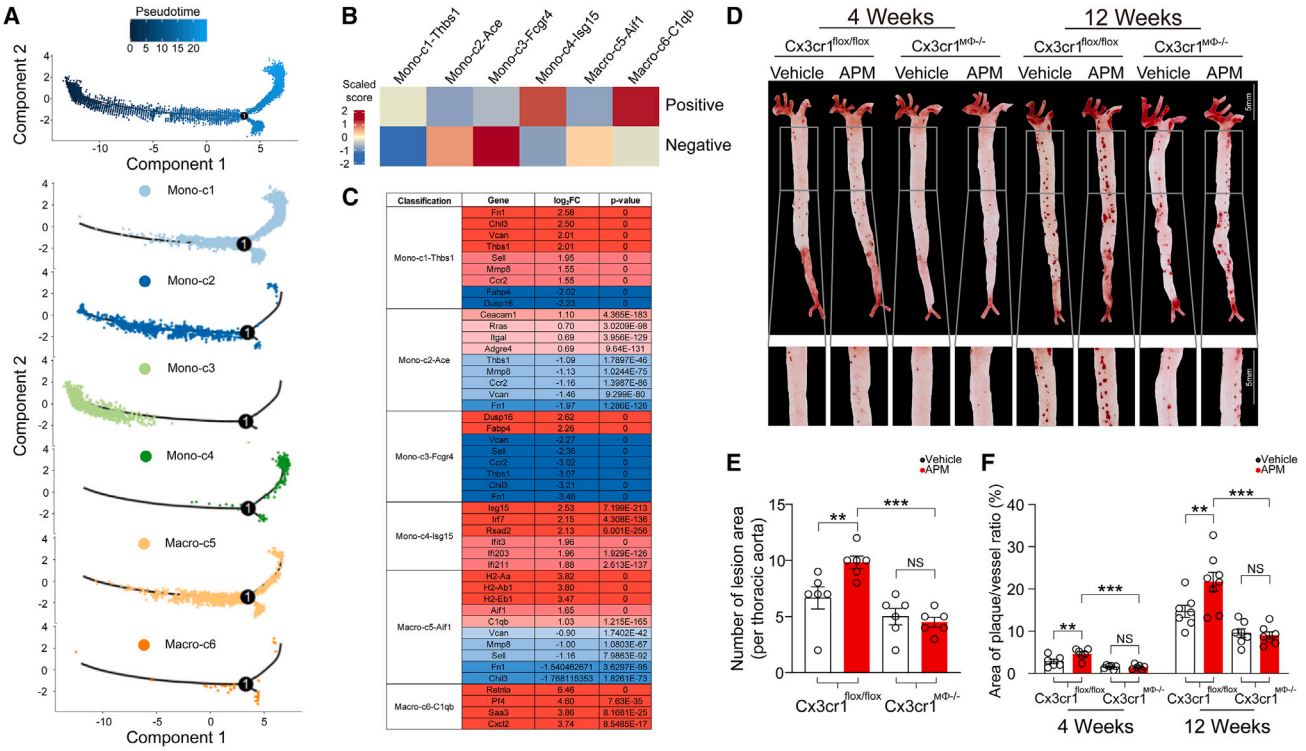

Figure 7. Genetic loss of function of *Cx3cr1* in monocytes/macrophages neutralizes APM-exacerbated atherosclerosis

(A) Pseudotime analysis of monocyte/macrophage differentiation indicates the differentiation order: Mono-c3 to Mono-c2 to Mono-c1 to Mono-c4. Mono-c3 and Mono-c1/c4 represent two polarized cell populations (n = 3 samples/group).

(B) GO enrichment scores proinflammatory and anti-inflammatory monocytes/macrophages (n = 3 samples/group).

(C) Differentially expressed genes shown by heatmap analysis in monocytes. Red color indicates high expression, and blue color indicates low expression of the relevant genes (n = 3 samples/group).

(D–F) Gross examination and quantification of positive signals of oil-red-O-stained aortas of Cx3cr1$^{M\Phi-/-}$/ApoE$^{-/-}$ double-knockout mice at the end of weeks 4 and 12 after aspartame (APM) feeding (n = 6–8 mice/group). ApoE$^{-/-}$ mice without genetic manipulation of the *Cx3cr1* gene served as a positive control. Vehicle feeding served as a negative control. Scale bar, 5 mm.

Data are presented as mean ± SEM. APM, aspartame.

(E and F) One-way ANOVA. **p < 0.01; ***p < 0.001. NS, not significant.

DISCUSSION

Understanding the mechanisms that underlie the exacerbation of atherosclerosis by ASWs is crucial for CVD prevention and treatment. The discovery of APM in elevating circulating insulin levels was unanticipated because blood glucose has been believed to be the key determinant of insulin secretion.[40] The role of parasympathetic activation of the vagus nerve in controlling insulin secretion was first reported more than 50 years ago.[41] Our present findings support this important pathway in regulation of insulin secretion. The fact that bilateral SDV completely abolishes the APM-induced insulin secretion supports the non-glucose pathway in mediating insulin secretion. Although the molecular mechanism was not fully elucidated in this study, ASWs, such as APM, likely activate luminal STRs distributed in the small intestine and potentially modulate insulin secretion. It seems that this mechanism commonly occurs in rodents and primates. In support of this notion, we show that APM effectively induces insulin secretion in both mice and monkeys.

A similar regulatory mechanism of insulin secretion most likely also exists in humans, as ASW consumption stimulates release of pancreatic insulin.[24,42] We should emphasize that we used only APM in our current study, which may not represent all non-nutritive sweeteners because their structures, modes of action, metabolism, and underlying mechanisms differ from each other. The impact of non-APM sweeteners on atherosclerosis and CVD warrants further investigation. Although not validated in this study, the effects of ASWs on insulin secretion, insulin sensitivity, and glucose tolerance have been previously investigated. For example, a randomized controlled trial in healthy human participants shows that sucralose, another commonly used non-nutritive ASW, significantly mitigates insulin sensitivity and increases an acute insulin response to glucose.[43] Such effects are likely to be augmented by the consumption of other ASWs including APM.

Insulin acts on numerous cell types to display its broad biological functions.[44] Among the target cells, ECs constituting the inner lining of vascular walls are probably the initial cell type that sensitizes to fluctuation in the circulating insulin. Thus, luminal ECs in the arterial wall likely trigger the initial response to the increased circulating insulin levels, and this early response subsequently provokes other pathological changes. In support of

Please cite this article in press as: Wu et al., Sweetener aspartame aggravates atherosclerosis through insulin-triggered inflammation, Cell Metabolism (2025), https://doi.org/10.1016/j.cmet.2025.01.006

this idea, our present findings showed that the CX3CL1 chemokine was the most stably upregulated protein in PAECs in response to insulin. This finding is somewhat unexpected because CX3CL1 is a signaling molecule that mainly augments inflammatory response. Perhaps, under physiological conditions, CX3CL1 would cause austere inflammatory responses and endothelial damages. However, under pathophysiological conditions such as hypercholesterolemia and endothelial damages, high levels of CX3CL1 likely exacerbate pathological progression such as inflammation of vascular walls.

In light of this, we show that CX3CL1-instigated inflammation by myeloid cells is the key process of atherosclerosis in ApoE-deficient mice. Although the CX3CR1 is broadly expressed in various types of immune cells, monocytes/macrophages are probably the key cell type that mediates the early event of atherosclerosis. Indeed, monocytes/macrophages express high levels of CX3CR1 that mediates CX3CL1-induced chemotaxis. CX3CL1 exhibits multifarious functions and certain unique features in target cells, including (1) membrane-bound CX3CL1 that acts as a potent adhesion molecule in its producing cells. Luminal surface CX3CL1 molecules in the vascular endothelium effectively mediate the adhesion of circulating $CX3CR1^{+}$ myeloid cells to the ECs. SEM analysis of the arterial vessel wall supports this view. The adhesion of monocytes to ECs through the CX3CL1-CX3CR1 interaction is essentially required for the initial endothelial damage and the formation of atherosclerotic lesions in the arterial vessel wall. (2) Both soluble and membrane-bound factions of CX3CL1 molecules establish a chemoattractant gradient that attracts both nearby and distal $CX3CR1^{+}$ myeloid cells to CX3CL1-producing ECs. This is an effective mechanism for accumulate monocytes/macrophages at the endothelial layer, and (3) conversion of monocytes/macrophages into the pro-atherosclerotic M1 macrophages. We show that CX3CL1-CX3CR1 signaling effectively commits primary macrophages to exhibit the M1 phenotype. These unique features of CX3CL1-CX3CR1 signaling are unlikely to be replaced by other inflammatory chemokines and cytokines in aggravating vascular inflammation and atherosclerosis. Genetic deletion of the *Cx3cr1* gene, specifically in monocytes/macrophages, provides compelling evidence that CX3CR1 signaling in macrophages is responsible for APM-aggravated atherosclerosis. Other gain-of-function and loss-of-function approaches further support the prominence of the EC-CX3CL1-macrophage-CX3CR1 signaling in atherosclerosis.

Although we focus on the APM-instigated insulin in exacerbating atherosclerosis in this study, we believe that the high insulin-CX3CL1-CX3CR1 signaling axis also significantly contributes to vascular inflammation and atherosclerosis in other pathological settings. For example, hyperinsulinemia in T2DM and in drug-associated adverse effects are probably causatively linked to high incidences of CVD and atherosclerosis-related cerebral disease. In fact, T2DM as a common metabolic disorder is known to predispose individuals to atherosclerotic CVD and cerebral disease. Feeding $ApoE^{-/-}$ mice with sucrose, which elevates blood insulin levels, also aggravates atherosclerosis, albeit with a slight delay AP formation relative to the APM group. These findings support the hypothesis that high levels of blood insulin exacerbate AP formation and growth under other pathophysiological conditions. At the time of this writing, we do not know the mechanistic differences between APM- and high-glucose-induced atherosclerosis. We speculate that in addition to insulin, various metabolites of APM and glucose may also participate in atherosclerosis-promoting effects. This interesting point warrants further investigation. Another interesting finding of our study is the difference in blood glucose levels between APM-fed mice and monkeys. While blood glucose levels remain unchanged in APM-fed mice, monkeys show marked decreases in blood glucose levels. In theory, blood glucose levels in both monkeys and mice should decrease due to increased insulin levels. Obviously, metabolic profiles of APM-feeding-triggered responses are likely different regarding to changes in blood glucose. Another possibility of causing immediate insulin resistance in experimental mice is probably associated with stress induced by experimental procedure. It is known that blood glucose levels in mice can be significantly influenced by stress induced by experimental procedure.[45] Both activation of the hypothalamic-pituitary-adrenal axis and the autonomic nervous system have been associated with experimental-procedure-induced increase in blood glucose.[46,47] In contrast to mouse models, the experimental procedure of monkeys involves less stressful handling using anesthesia prior to collection of samples. These aspects may partly explain the difference between mouse and monkey glucose levels in response to APM-augmented insulin.

The discovery of the insulin-CX3CL1-CX3CR1 signaling axis in exacerbating atherosclerosis not only provides compelling mechanistic insights into ASW-associated CVDs but also defines therapeutic targets for treatment of atherosclerosis-associated diseases such as CVD and stroke. Development of neutralizing agents that block the functions of CX3CL1 or CX3CR1 offers a new therapeutic option for treating and preventing these most common and lethal diseases in human patients.

Limitations of the study

Several limitations exist in this study, including (1) although APM is one of the most common sweeteners studied in our current work, APM may not represent the effects of all other sweeteners that are consumed daily in various foods and beverages; (2) concerning the $ApoE^{-/-}$ mouse model, this animal model may not fully be relevant to the onset and development of human atherosclerosis. The $ApoE^{-/-}$ mice display perturbed lipid metabolism and inflammation. Furthermore, feeding $ApoE^{-/-}$ mice with a high-fat, high-CHOL diet also diminishes clinical relevance; (3) although a monkey model has been used to validate our findings in mouse models, human relevance warrants a rigorously designed clinical investigation to obtain definite conclusions; (4) in the monkey model, owing to technical difficulties and feasibilities, our current work did not include the impact of APM on atherosclerosis; and (5) according to our current data, we cannot exclude other mechanisms that are independent of the STR. Nonetheless, further studies should consider these important issues.

RESOURCE AVAILABILITY

Lead contact

Further information and requests for resources and reagents should be directed to and will be facilitated by the lead contact Yihai Cao (yihai.cao@ki.se).

Materials availability

This study did not generate new unique reagents.

Data and code availability

- Source data and uncropped blots are provided in Data S1.
- No original code was generated in this study.
- Any additional information required to reanalyze the data reported in this paper is available from the lead contact upon request.

ACKNOWLEDGMENTS

Y. Cao's laboratory is supported through research grants from the Swedish Cancer Foundation, the Strategic Research Areas (SFO)–Stem Cell and Regenerative Medicine Foundation, the Karolinska Institute Foundation, the NOVO Nordisk Foundation, the Swedish Research Council (project no. 2016-02215, project no. 2019-01502, and project no. 2021-06122), the Swedish Research Council-the National Natural Science Foundation of China joint grants, the Hong Kong Centre for Cerebro-Cardiovascular Health Engineering, and the Horizon Europe grant-PERSEUS (action number: 101099423). State Key Laboratory for Innovation and Transformation of Luobing Theory is supported through research grants from Key R&D Program of Shandong Province (2021SFGC0503, 2021ZLGX02, 2021ZDSYS05), the National Natural Science Foundation of China (82241203, 82030051), State Key R&D Program of China (2021YFF0501403), and the Taishan Scholars Program of Shandong Province (to C. Zhang).

AUTHOR CONTRIBUTIONS

Y. Cao generated the initial idea of this project. Y. Cao designed the study, supervised experimentalists, and analyzed the data. Y. Cao wrote the manuscript. W.W. performed most experiments, collected all the data, participated in analysis of results, and formulated the data into publishable figures. W.W. contributed to description of methodologies. W.S., S.C., and W.X. participated in experimentation and data analysis. Yun Zhang, C. Zhang, and Y. Chen significantly contributed to project discussion and material supply. J.J., L.Y., G.Y., S.L., Z.G., Yuan Zhang, W.J., X.J., X.W., Q.W., X.Y., W.T., and C. Zhao participated in project discussion and data analysis.

DECLARATION OF INTERESTS

The authors declare no competing interests.

STAR★METHODS

Detailed methods are provided in the online version of this paper and include the following:

SUPPLEMENTAL INFORMATION

Supplemental information can be found online at https://doi.org/10.1016/j.cmet.2025.01.006.

Received: May 30, 2024
Revised: October 23, 2024
Accepted: January 8, 2025
Published: February 19, 2025

REFERENCES

1. Mallikarjun, S., and Sieburth, R.M. (2015). Aspartame and risk of cancer: A meta-analytic review. Arch. Environ. Occup. Health *70*, 133–141. https://doi.org/10.1080/19338244.2013.828674.
2. Czarnecka, K., Pilarz, A., Rogut, A., Maj, P., Szymańska, J., Olejnik, Ł., and Szymański, P. (2021). Aspartame-true or false? Narrative review of safety analysis of general use in products. Nutrients *13*, 1957. https://doi.org/10.3390/nu13061957.
3. Choudhary, A.K., and Lee, Y.Y. (2018). The debate over neurotransmitter interaction in aspartame usage. J. Clin. Neurosci. *56*, 7–15. https://doi.org/10.1016/j.jocn.2018.06.043.
4. Oyama, Y., Sakai, H., Arata, T., Okano, Y., Akaike, N., Sakai, K., and Noda, K. (2002). Cytotoxic effects of methanol, formaldehyde, and formate on dissociated rat thymocytes: a possibility of aspartame toxicity. Cell Biol. Toxicol. *18*, 43–50. https://doi.org/10.1023/a:1014419229301.
5. Debras, C., Chazelas, E., Sellem, L., Porcher, R., Druesne-Pecollo, N., Esseddik, Y., de Edelenyi, F.S., Agaësse, C., De Sa, A., Lutchia, R., et al. (2022). Artificial sweeteners and risk of cardiovascular diseases: results from the prospective NutriNet-Sante cohort. BMJ *378*, e071204. https://doi.org/10.1136/bmj-2022-071204.
6. Fowler, S.P.G. (2016). Low-calorie sweetener use and energy balance: results from experimental studies in animals, and large-scale prospective studies in humans. Physiol. Behav. *164*, 517–523. https://doi.org/10.1016/j.physbeh.2016.04.047.
7. Marinovich, M., Galli, C.L., Bosetti, C., Gallus, S., and La Vecchia, C. (2013). Aspartame, low-calorie sweeteners and disease: regulatory safety and epidemiological issues. Food Chem. Toxicol. *60*, 109–115. https://doi.org/10.1016/j.fct.2013.07.040.
8. Pearlman, M., Obert, J., and Casey, L. (2017). The association between artificial sweeteners and obesity. Curr. Gastroenterol. Rep. *19*, 64. https://doi.org/10.1007/s11894-017-0602-9.
9. Suez, J., Korem, T., Zeevi, D., Zilberman-Schapira, G., Thaiss, C.A., Maza, O., Israeli, D., Zmora, N., Gilad, S., Weinberger, A., et al. (2014). Artificial sweeteners induce glucose intolerance by altering the gut microbiota. Nature *514*, 181–186. https://doi.org/10.1038/nature13793.
10. Swithers, S.E. (2013). Artificial sweeteners produce the counterintuitive effect of inducing metabolic derangements. Trends Endocrinol. Metab. *24*, 431–441. https://doi.org/10.1016/j.tem.2013.05.005.
11. Swithers, S.E. (2015). Not so sweet revenge: unanticipated consequences of high-intensity sweeteners. Behav. Anal. *38*, 1–17. https://doi.org/10.1007/s40614-015-0028-3.
12. Swithers, S.E. (2016). Not-so-healthy sugar substitutes? Curr. Opin. Behav. Sci. *9*, 106–110. https://doi.org/10.1016/j.cobeha.2016.03.003.

13. Ruiz-Ojeda, F.J., Plaza-Díaz, J., Sáez-Lara, M.J., and Gil, A. (2019). Effects of sweeteners on the gut microbiota: a review of experimental studies and clinical trials. Adv. Nutr. *10*, S31–S48. https://doi.org/10.1093/advances/nmy037.

14. Pang, M.D., Goossens, G.H., and Blaak, E.E. (2020). The impact of artificial sweeteners on body weight control and glucose homeostasis. Front. Nutr. *7*, 598340. https://doi.org/10.3389/fnut.2020.598340.

15. Peters, J.C., Beck, J., Cardel, M., Wyatt, H.R., Foster, G.D., Pan, Z., Wojtanowski, A.C., Vander Veur, S.S., Herring, S.J., Brill, C., et al. (2016). The effects of water and non-nutritive sweetened beverages on weight loss and weight maintenance: A randomized clinical trial. Obesity (Silver Spring) *24*, 297–304. https://doi.org/10.1002/oby.21327.

16. Tzagournis, M., Chiles, R., Ryan, J.M., and Skillman, T.G. (1968). Interrelationships of hyperinsulinism and hypertriglyceridemia in young patients with coronary heart disease. Circulation *38*, 1156–1163. https://doi.org/10.1161/01.cir.38.6.1156.

17. Després, J.P., Lamarche, B., Mauriège, P., Cantin, B., Dagenais, G.R., Moorjani, S., and Lupien, P.J. (1996). Hyperinsulinemia as an independent risk factor for ischemic heart disease. N. Engl. J. Med. *334*, 952–957. https://doi.org/10.1056/NEJM199604113341504.

18. Lakka, H.M., Lakka, T.A., Tuomilehto, J., Sivenius, J., and Salonen, J.T. (2000). Hyperinsulinemia and the risk of cardiovascular death and acute coronary and cerebrovascular events in men: the Kuopio ischaemic Heart Disease Risk Factor Study. Arch. Intern. Med. *160*, 1160–1168. https://doi.org/10.1001/archinte.160.8.1160.

19. Sander, M., Griffen, S.C., Huang, J., and German, M.S. (1998). A novel glucose-responsive element in the human insulin gene functions uniquely in primary cultured islets. Proc. Natl. Acad. Sci. USA *95*, 11572–11577. https://doi.org/10.1073/pnas.95.20.11572.

20. Irwin, N., McClean, P.L., Harriott, P., and Flatt, P.R. (2007). Beneficial effects of sub-chronic activation of glucagon-like peptide-1 (GLP-1) receptors on deterioration of glucose homeostasis and insulin secretion in aging mice. Exp. Gerontol. *42*, 296–300. https://doi.org/10.1016/j.exger.2006.10.017.

21. Itoh, Y., Kawamata, Y., Harada, M., Kobayashi, M., Fujii, R., Fukusumi, S., Ogi, K., Hosoya, M., Tanaka, Y., Uejima, H., et al. (2003). Free fatty acids regulate insulin secretion from pancreatic beta cells through GPR40. Nature *422*, 173–176. https://doi.org/10.1038/nature01478.

22. Meyers, E.E., Kronemberger, A., Lira, V., Rahmouni, K., and Stauss, H.M. (2016). Contrasting effects of afferent and efferent vagal nerve stimulation on insulin secretion and blood glucose regulation. Physiol. Rep. *4*, e12718. https://doi.org/10.14814/phy2.12718.

23. Buchanan, K.L., Rupprecht, L.E., Kaelberer, M.M., Sahasrabudhe, A., Klein, M.E., Villalobos, J.A., Liu, W.W., Yang, A., Gelman, J., Park, S., et al. (2022). The preference for sugar over sweetener depends on a gut sensor cell. Nat. Neurosci. *25*, 191–200. https://doi.org/10.1038/s41593-021-00982-7.

24. Mathur, K., Agrawal, R.K., Nagpure, S., and Deshpande, D. (2020). Effect of artificial sweeteners on insulin resistance among type-2 diabetes mellitus patients. J. Fam. Med. Prim. Care *9*, 69–71. https://doi.org/10.4103/jfmpc.jfmpc_329_19.

25. Gerspach, A.C., Steinert, R.E., Schönenberger, L., Graber-Maier, A., and Beglinger, C. (2011). The role of the gut sweet taste receptor in regulating GLP-1, PYY, and CCK release in humans. Am. J. Physiol. Endocrinol. Metab. *301*, E317–E325. https://doi.org/10.1152/ajpendo.00077.2011.

26. Frank, G.K.W., Oberndorfer, T.A., Simmons, A.N., Paulus, M.P., Fudge, J.L., Yang, T.T., and Kaye, W.H. (2008). Sucrose activates human taste pathways differently from artificial sweetener. Neuroimage *39*, 1559–1569. https://doi.org/10.1016/j.neuroimage.2007.10.061.

27. Orskov, C., Wettergren, A., and Holst, J.J. (1996). Secretion of the incretin hormones glucagon-like peptide-1 and gastric inhibitory polypeptide correlates with insulin secretion in normal man throughout the day. Scand. J. Gastroenterol. *31*, 665–670. https://doi.org/10.3109/00365529609009147.

28. Ramracheya, R.D., McCulloch, L.J., Clark, A., Wiggins, D., Johannessen, H., Olsen, M.K., Cai, X., Zhao, C.M., Chen, D., and Rorsman, P. (2016). PYY-Dependent Restoration of Impaired insulin and glucagon Secretion in type 2 diabetes following Roux-En-Y Gastric Bypass Surgery. Cell Rep. *15*, 944–950. https://doi.org/10.1016/j.celrep.2016.03.091.

29. Howard, G., O'Leary, D.H., Zaccaro, D., Haffner, S., Rewers, M., Hamman, R., Selby, J.V., Saad, M.F., Savage, P., and Bergman, R. (1996). Insulin sensitivity and atherosclerosis. The insulin resistance atherosclerosis study (IRAS) investigators. Circulation *93*, 1809–1817. https://doi.org/10.1161/01.cir.93.10.1809.

30. Libby, P., Buring, J.E., Badimon, L., Hansson, G.K., Deanfield, J., Bittencourt, M.S., Tokgözoğlu, L., and Lewis, E.F. (2019). Atherosclerosis. Nat. Rev. Dis. Primers *5*, 56. https://doi.org/10.1038/s41572-019-0106-z.

31. Ginsberg, H.N. (2000). Insulin resistance and cardiovascular disease. J. Clin. Invest. *106*, 453–458. https://doi.org/10.1172/JCI10762.

32. Libby, P., Ridker, P.M., and Maseri, A. (2002). Inflammation and atherosclerosis. Circulation *105*, 1135–1143. https://doi.org/10.1161/hc0902.104353.

33. Mestas, J., and Ley, K. (2008). Monocyte-endothelial cell interactions in the development of atherosclerosis. Trends Cardiovasc. Med. *18*, 228–232. https://doi.org/10.1016/j.tcm.2008.11.004.

34. Kataoka, N., Iwaki, K., Hashimoto, K., Mochizuki, S., Ogasawara, Y., Sato, M., Tsujioka, K., and Kajiya, F. (2002). Measurements of endothelial cell-to-cell and cell-to-substrate gaps and micromechanical properties of endothelial cells during monocyte adhesion. Proc. Natl. Acad. Sci. USA *99*, 15638–15643. https://doi.org/10.1073/pnas.242590799.

35. Bentzon, J.F., Otsuka, F., Virmani, R., and Falk, E. (2014). Mechanisms of plaque formation and rupture. Circ. Res. *114*, 1852–1866. https://doi.org/10.1161/CIRCRESAHA.114.302721.

36. Swithers, S.E., Sample, C.H., and Davidson, T.L. (2013). Adverse effects of high-intensity sweeteners on energy intake and weight control in male and obesity-prone female rats. Behav. Neurosci. *127*, 262–274. https://doi.org/10.1037/a0031717.

37. Bachmanov, A.A., Tordoff, M.G., and Beauchamp, G.K. (2001). Sweetener preference of C57BL/6ByJ and 129P3/J mice. Chem. Senses *26*, 905–913. https://doi.org/10.1093/chemse/26.7.905.

38. Wojdasiewicz, P., Poniatowski, L.A., Kotela, A., Deszczyński, J., Kotela, I., and Szukiewicz, D. (2014). The chemokine CX3CL1 (fractalkine) and its receptor CX3CR1: occurrence and potential role in osteoarthritis. Arch. Immunol. Ther. Exp. (Warsz) *62*, 395–403. https://doi.org/10.1007/s00005-014-0275-0.

39. Apostolakis, S., and Spandidos, D. (2013). Chemokines and atherosclerosis: focus on the CX3CL1/CX3CR1 pathway. Acta Pharmacol. Sin. *34*, 1251–1256. https://doi.org/10.1038/aps.2013.92.

40. Fu, Z., Gilbert, E.R., and Liu, D. (2013). Regulation of insulin synthesis and secretion and pancreatic Beta-cell dysfunction in diabetes. Curr. Diabetes Rev. *9*, 25–53. https://doi.org/10.2174/157339913804143225.

41. Frohman, L.A., Ezdinli, E.Z., and Javid, R. (1967). Effect of vagotomy and vagal stimulation on insulin secretion. Diabetes *16*, 443–448. https://doi.org/10.2337/diab.16.7.443.

42. Malaisse, W.J., Vanonderbergen, A., Louchami, K., Jijakli, H., and Malaisse-Lagae, F. (1998). Effects of artificial sweeteners on insulin release and cationic fluxes in rat pancreatic islets. Cell. Signal. *10*, 727–733. https://doi.org/10.1016/s0898-6568(98)00017-5.

43. Romo-Romo, A., Aguilar-Salinas, C.A., Brito-Córdova, G.X., Gómez-Díaz, R.A., and Almeda-Valdes, P. (2018). Sucralose decreases insulin sensitivity in healthy subjects: a randomized controlled trial. Am. J. Clin. Nutr. *108*, 485–491. https://doi.org/10.1093/ajcn/nqy152.

44. Wilcox, G. (2005). Insulin and insulin resistance. Clin. Biochem. Rev. *26*, 19–39.

45. Ghosal, S., Nunley, A., Mahbod, P., Lewis, A.G., Smith, E.P., Tong, J., D'Alessio, D.A., and Herman, J.P. (2015). Mouse handling limits the impact of stress on metabolic endpoints. Physiol. Behav. *150*, 31–37. https://doi.org/10.1016/j.physbeh.2015.06.021.

46. Ghalami, J., Zardooz, H., Rostamkhani, F., Farrokhi, B., and Hedayati, M. (2013). Glucose-stimulated insulin secretion: effects of high-fat diet and acute stress. J. Endocrinol. Invest. *36*, 835–842. https://doi.org/10.3275/8959.

47. Thorens, B. (2011). Brain glucose sensing and neural regulation of insulin and glucagon secretion. Diabetes Obes. Metab. *13*, 82–88. https://doi.org/10.1111/j.1463-1326.2011.01453.x.

48. Stuart, T., Butler, A., Hoffman, P., Hafemeister, C., Papalexi, E., Mauck, W.M., 3rd, Hao, Y., Stoeckius, M., Smibert, P., and Satija, R. (2019). Comprehensive integration of single-cell data. Cell *177*, 1888–1902.e21. https://doi.org/10.1016/j.cell.2019.05.031.

49. Germain, P.L., Lun, A., Garcia Meixide, C., Macnair, W., and Robinson, M.D. (2021). Doublet identification in single-cell sequencing data using scDblFinder. F1000Res *10*, 979. https://doi.org/10.12688/f1000research.73600.2.

50. Yu, G., Wang, L.G., Han, Y., and He, Q.Y. (2012). clusterProfiler: an R package for comparing biological themes among gene clusters. Omics *16*, 284–287. https://doi.org/10.1089/omi.2011.0118.

51. Hänzelmann, S., Castelo, R., and Guinney, J. (2013). GSVA: gene set variation analysis for microarray and RNA-seq data. BMC Bioinformatics *14*, 7. https://doi.org/10.1186/1471-2105-14-7.

52. Qiu, X., Mao, Q., Tang, Y., Wang, L., Chawla, R., Pliner, H.A., and Trapnell, C. (2017). Reversed graph embedding resolves complex single-cell trajectories. Nat. Methods *14*, 979–982. https://doi.org/10.1038/nmeth.4402.

Please cite this article in press as: Wu et al., Sweetener aspartame aggravates atherosclerosis through insulin-triggered inflammation, Cell Metabolism (2025), https://doi.org/10.1016/j.cmet.2025.01.006

STAR★METHODS

KEY RESOURCES TABLE

REAGENT or RESOURCE	SOURCE	IDENTIFIER
Antibodies		
Rabbit anti-mouse α-SMA antibody	Cell Signaling	Cell Signaling: Cat# 19245; RRID: AB_2734735
Rat anti-mouse MOMA-2 antibody	ABCAM	ABCAM: Cat# ab33451; RRID: AB_776518
Rabbit anti-mouse CX3CR1 antibody	ABCAM	ABCAM: Cat# ab308613; RRID: AB_3271513
Alexa Fluor 594-labeled goat anti-rabbit secondary antibody	ZSGB-BIO	ZSGB-BIO: Cat# ZF-0516; RRID: AB_2936330
FITC-labeled goat anti-rat secondary antibody	ZSGB-BIO	ZSGB-BIO: Cat# ZF-0315; RRID: AB_3662146
horseradish-labeled goat anti-rabbit	ZSGB-BIO	ZSGB-BIO: Cat# ZB-2301; RRID: AB_2747412
Rabbit anti-mouse CX3CL1 antibody	Immunoway	Immunoway: Cat# YT5354; RRID: AB_3662153
CD16/32	Biolegend	Biolegend: Cat#101319; RRID: AB_1574973
PE-conjugated CD31 antibody	Invitrogen	Invitrogen: Cat# 12-0311-82; RRID: AB_465632
FITC-conjugated CD45 antibody	Invitrogen	Invitrogen: Cat# 11-0451-82; RRID: AB_465050
Rabbit anti-mouse CX3CL1 APC-conjugated monoclonal antibody	RnD system	RnD system: Cat# FAB571A; RRID: AB_3662161
Chemicals, peptides, and recombinant proteins		
recombinant CX3CL1 protein	Sino Biological	Sino Biological: Cat# 50917-M08Y
crystal violet	KeyGEN	KeyGEN: Cat# KGA229
insulin	Sigma	Sigma: Cat# I9278
Calcein AM	Beyotime	Beyotime: Cat# C2012
quick antigen retrieval solution for frozen	Beyotime	Beyotime: Cat# P0090
peptone	Solarbio	P8450
beef extract	Solarbio	G8270
starch soluble	Solarbio	G8300
NaCl	SCR	10019318
glutaraldehyde	Coolaber	Coolaber: Cat# SL1770
osmic acid	Ted Pella 642 Inc	Ted Pella 642 Inc: Cat# 18456
Isoamyl acetate	Sinopharm Chemical Reagent Co. Ltd.	Sinopharm Chemical Reagent Co. Ltd.: Cat# 10003128
Critical Point Dryers	Quorum	Quorum: Cat# K850
ion sputter coater	HITACHI	HITACHI: Cat# MC1000
Epon812	SPI	SPI: Cat# 90529-77-4
HISTOPAQUE	Sigma-Aldrich	Sigma-Aldrich: Cat# 10771
RBC lysis buffer	Miltenyi	Miltenyi: Cat# 130-094-183
Oil Red O	Servicebio	Servicebio: Cat# G1015
HiScript III RT SuperMix for qPCR	Vazyme	Vazyme: Cat# R323-01
ChamQ Universal SYBR qPCR Master Mix	Vazyme	Vazyme: Cat# Q711
Matirgel	Coning	Coning: Cat# 356230
Trizol	CWbio	CWbio: Cat#: 01761/40523

(*Continued on next page*)

Please cite this article in press as: Wu et al., Sweetener aspartame aggravates atherosclerosis through insulin-triggered inflammation, Cell Metabolism (2025), https://doi.org/10.1016/j.cmet.2025.01.006

Continued

REAGENT or RESOURCE	SOURCE	IDENTIFIER
goat serum	Gene Tech	Gene Tech: Cat# GK500710
Sirius-red-staining-solution	Science Phygene	Science Phygene: Cat# PH1098
type I collagenase	Worthington	Worthington: Cat# LS004194
type II collagenase	Worthington	Worthington: Cat# LS004174
phosphate buffered saline	Thermo Fisher	Thermo Fisher: Cat# 10010023
pentobarbital sodium	Notlas	Notlas: Cat# 57-33-0
M5 HiPer ECL Western HRP Substrate	Mei5 Biotech	Mei5 Biotech: Cat# MF074-05
endothelial cell specific culture medium	Procell	Procell: Cat# CM-M075
Critical commercial assays		
DAPI	ABCAM	ABCAM: Cat# ab104139
Mouse Fractalkine (CX3CL1) ELISA Kit	ABCAM	ABCAM: Cat# ab100683
Fastagen RNAfast200 kit	Fastagen	Fastagen: Cat# 220011
Ultrasensitive mouse insulin ELISA	Mercodia	Mercodia: Cat# 10-1249-01
Monkey insulin ELISA	Arigo	Arigo: Cat# ARG82671
Hematoxylin-Eosin Stain Kit	Solarbio	Solarbio: Cat# G1120
Mouse/Rat C-Peptide ELISA Kit	RayBiotech	RayBiotech: Cat# EIAM-CPE
Cynomolgus Monkey C-Peptide ELISA Kit	NOVUS	NOVUS: Cat# NBP2-59957
Deposited data		
Singel cell sequencing raw data in PBMC	GSE282569	N/A
Source data	N/A	Data S1- Source data
RNA-seq	N/A	Data S1 – RNA-seq
Experimental models: Cell lines		
RAW 264.7	ICell Bioscience Inc	ICell Bioscience Inc: Cat# iCell-m047
Experimental models: Organisms/strains		
C57BL/6J	Beijing Vital River Laboratory Animal Technology Co. Ltd	Beijing Vital River Laboratory Animal Technology: Cat# 213
ApoE $^{-/-}$ C57BL/6J	GemPharmatech Co. Ltd.	GemPharmatech: Cat# T001458
Cx3cr1 $^{flox/flox}$	GemPharmatech Co. Ltd.	GemPharmatech: Cat# T005904
Lyz2-cre C57BL/6J	GemPharmatech Co. Ltd.	GemPharmatech: Cat# T003822
cynomolgus monkey	Guangxi Bomai Biotechnology Co. Ltd.	N/A
Oligonucleotides		
Primers for qPCR	See Table S1 – this paper	N/A
pLV-hU6-CX3CR1 shRNA-hef1a-mNeongreen-P2A-Puro	SyngenTech	pHS-ASR-2824
Plv-hU6-NC shRNA-hef1a-mNeogreen-P2A-Puro	SyngenTech	pHS-ASR-LW429
Software and algorithms		
FlowJo v10.8.1	TreeStar	RRID: SCR_008520
ImageJ	NIH	RRID: SCR_003070
GraphPad Prism v8.2.1.441	GraphPad	RRID: SCR_002798
SPSS v26.0	IBM	RRID: SCR_002865
R v4.3.1	R	RRID: SCR_001905
Other		
parallel-plate flow chambers	ibidi	Ibidi: Cat# 80176
transwells	Corning	Corning: Cat# 3422
scanning electron microscope	HITACHI	HITACHI: Model. SU8100
transmission electron microscope	HITACHI	HITACHI: Model. HT7800
CLAMS	Columbus Instruments	N/A
Light Cycler 480 instrument	Roche	N/A

(*Continued on next page*)

Please cite this article in press as: Wu et al., Sweetener aspartame aggravates atherosclerosis through insulin-triggered inflammation, Cell Metabolism (2025), https://doi.org/10.1016/j.cmet.2025.01.006

CellPress
OPEN ACCESS

Continued

REAGENT or RESOURCE	SOURCE	IDENTIFIER
Accu-Chek glucose meter	Roche Diagnostics	N/A
hair removal cream	Veet	Veet: Cat# 3228470
mini-osmotic pump	ALZET	ALZET: Cat# 2004
High-fat, high-cholesterol diet	Trophic Animal Feed High-Tech Co. Ltd	Trophic: Cat# TP28521
Aspartame	Jiang su ke lai rui kang Co. Ltd.	N/A
Glucose monohydrate	HUSHI	HUSHI: Cat# 10010518
Novolin 30R	Novo Nordisk	Novo Nordisk: Cat# 8-0267-03-260-1

EXPERIMENTAL MODEL AND STUDY PARTICIPANT DETAILS

Mice

Wild-type male C57BL/6J mice, male and female ApoE$^{-/-}$ C57BL/6J mice, aged 6-8 weeks, were purchased from the Beijing Vital River Laboratory Animal Technology Co., Ltd. (China) and GemPharmatech Co., Ltd. (Nanjing, China), respectively. Cx3cr1$^{flox/flox}$ mice were created by insertion of *LoxP* sites flanking the *Cx3cr1* gene (Figure 6A). Transgenic mice carrying the lysozyme-driven Cre recombinase (*Lyz2*-Cre) were purchased from the GemPharmatech Co., Ltd. The Cx3cr1$^{flox/flox}$ mice and *Lyz2*-Cre mice were crossed to obtain the Cx3cr1$^{M\Phi-/-}$ knockout mice with specific deletion of the *Cx3cr1* gene in monocytes/macrophages. The Cx3cr1$^{M\Phi-/-}$mice were further crossed with ApoE$^{-/-}$ mice to generate Cx3cr1$^{M\Phi-/-}$/ApoE$^{-/-}$ double-knockout mice. All experimental mice, including ApoE$^{-/-}$, and Cx3cr1$^{M\Phi-/-}$/ApoE$^{-/-}$ double-knockout mice, were fed with high-fat, high-cholesterol diet (HFCD, Trophic Animal Feed High-Tech Co., Ltd., China). Wild-type male C57BL/6J mice for acute experiments and primary cell culture were fed regular chow diet. Regarding to HFCD, the mice were fed HFCD with an energy-free vehicle, APM, or sucrose at the indicated time-points of various experimental groups. Prior to and after random grouping, all mice were kept at 22°C with 50%-60% humidity, in a specific pathogen-free controlled environment, and a standard 12-h light and 12-h dark cycle as the housekeeping conditions. All mice were healthy and received no treatments other than those described in this study. All mouse experiments were performed according to the guidelines of the Management Rules of the Chinese Ministry of Health (MRCMH) and local ethical permissions approved by the Local Ethical Committee of the Qilu Hospital, Shandong University.

Monkey

Male 4-year-old cynomolgus monkeys were purchased from the Guangxi Bomai Biotechnology Co., Ltd. These monkeys were healthy and received no treatments with drugs or interventions other than the experimental procedures described in this study. Unlike the mouse study, all monkeys did not receive HFCD feeding in all experimental groups. Each of the experimental monkeys was individually caged, randomly grouped, and either APM or sucrose was added to their drinking water. Prior to and after random grouping, all monkeys were kept at 18°C with 73% humidity, under a standard environment with 12-h light and 12-h dark cycle as the housekeeping conditions. The monkey experiments were also performed according to the guidelines of the Management Rules of the Chinese Ministry of Health (MRCMH) and local ethical permissions approved by the Local Ethical Committee of the Qilu Hospital, Shandong University.

Isolation of primary macrophages

Prior to harvesting primary macrophages, each of wild-type male C57BL/6J mice at the age of 6-8 weeks, received intraperitoneal injection of a 2 mL 3% broth starch containing 2 g peptone (Cat. P8450, Solarbio, China), 0.6 g beef extract (Cat. G8270, Solarbio, China), 12 g starch soluble (Cat. G8300, Solarbio, China), and 1 g NaCl (Cat. 10019318, SCR, China). Because there were no sex differences of mice in our experimental settings, we used male mice for most of our experiments owing to the availability of male mice in our animal facility. After 3 days of injection, the mice were anesthetized and the peritoneum of each animal was surgically exposed. Each exposed peritoneal cavity received injection of 8 mL culture medium, followed by re-collection of the injected medium. This procedure was repeatedly performed 3 times and the pooled macrophage-containing medium was harvested by centrifugation. Primary macrophages were suspended at 5×10^6 cells/mL in a DMEM medium containing 10% FBS and seeded in 6-well plates at a cell density of 1×10^7. Cells were cultured at 37°C in a humidified atmosphere with 5% CO_2.

METHOD DETAILS

Acute and long-term treatment with APM

In acute experiments, wild-type male C57BL/6J mice were fasted and water-deprived for 12 hours as preparation. Each mouse was orally fed with 200μL of distilled water containing vehicle or different concentrations of APM (0.05%, 0.1% or 0.15%, w/w) by dropping the solution onto the mouse's face. After feeding, we waited for 30 minutes. Plasma samples were collected from each eye socket using EDTA-treated tubes for insulin and C-peptide level assays.

Please cite this article in press as: Wu et al., Sweetener aspartame aggravates atherosclerosis through insulin-triggered inflammation, Cell Metabolism (2025), https://doi.org/10.1016/j.cmet.2025.01.006

In long-term-treated experiments, HFCD alone groups served as non-treated vehicle controls. HFCD plus 15% sucrose or 0.15% APM (w/w) were defined as treated groups. ApoE$^{-/-}$ C57BL/6J mice were maintained on this special type of HFCD daily until the various time points of the experiment. Prior to the final day of experiments, the mice were fasted and water deprived for 12 hours as preparation. The blood was collected into coagulation-promoting tubes (Cat. 367955, Becton Dickinson and Company, USA) and centrifuged to obtain serum for subsequent assay.

Measurements of mouse respiratory metabolism

After 12 weeks of HFCD feeding with vehicle, sucrose or APM, ApoE$^{-/-}$ mice were individually housed in the CLAMS system (Columbus Instruments) for 12 h-acclimation. Mice were kept at 22°C with 50%-60% humidity with a standard 12-h light/dark shift cycle for 24 h for measuring respiratory metabolism.

Subdiaphragmatic vagotomy

ApoE$^{-/-}$ C57BL/6J mice, aged 6-8-weeks, were anesthetized by intraperitoneal injection of pentobarbital sodium (Cat. 57-33-0, Notlas, China). Under anesthetized conditions, a 1.5 cm longitudinal incision by surgery was made, 0.5 cm distal to the xiphoid process of the sternum. Within this surgical incision, the stomach body was exposed and the vagus nerve located in the anterior and the right walls of the esophagus were transected. The operated mice were recovered in a warm environment. This surgical procedure was highly repeated with a very low mortality rate of mice. Again, the ethical permission of SDV procedures was approved by the Local Ethical Committee of the Qilu Hospital, Shandong University.

Subcutaneous insulin micropump implantation

The mini-osmotic pumps with a release rate 0.25 μL/h and a duration for 28 days were purchased from the ALZET company (Cat. 2004, USA). Within each mini-osmotic pump, 0.9% NaCl (saline) in 200 μL was loaded as the vehicle control or 1 mg/mL insulin (Cat. I9278, Sigma, Germany) in 200 μL solution in saline as the experimental group. Male ApoE$^{-/-}$ mice, aged 6-8 weeks, were anesthetized with pentobarbital sodium (1% pentobarbital sodium, 0.15 mL/mouse, Cat. 57-33-0, Notlas, China) for 2 h by intraperitoneal injection. During anesthesia, the fur on the back of each mouse was removed by a non-invasive method with a hair removal cream (Cat. 3228470, Veet, France). A transverse incision of 1.5 cm in length was surgically made by a pair of surgical scissors on the back neck of each mouse. Within this surgical wound, a pair of vascular forceps were used to bluntly dissect the skin and fascia tissues, followed by subcutaneously implanting a mini-osmotic pump into each mouse. After suturing, the operated mice were kept at a 30°C warm environment for recovery. The mini-osmotic pumps were kept in the mouse body for 28 days and were replaced with new pumps using the same procedure and the 28-day renewal period.

Acute experiment in monkeys

In acute experiments, male 4-year-old cynomolgus monkeys were fasted and water deprived for 12 h as preparation. Each monkey was fed with 330 mL of distilled water containing vehicle, 15% sucrose or 0.15% APM (w/w). After 10-min feeding, blood samples were collected at various time point (0, 30, 60, 90 and 120 min) into coagulation-promoting tubes to obtain serum for measurement of serum glucose, insulin and C-peptide levels.

Blood chemistry

Mouse and monkey serum was prepared in coagulation-promoting tubes (Cat. 367955, Becton, Dickinson and Company, USA). Mouse plasma was prepared in tube treated with EDTA. Serum levels of CHOL, LDL, TG, and HDL were measured using a Beckman AU5821 automatic biochemistry analyzer (Beckman, Co., Ltd., USA). Blood glucose strips and the Accu-Chek glucose meter (Roche Diagnostics, USA) were used to measure blood glucose levels (Cat. S0130, Sigma, Germany). Plasma or serum insulin levels were measured by commercially available ELISA kits (Cat. 10-1249-01, Mercodia, Sweden for mice; Cat. ARG82671, arigo, China for monkeys). Plasma or serum C-peptide levels were measured by ELISA kits (Cat. EIAM-CPE, RayBiotech, USA, for mice; Cat. NBP2-59957, NOVUS, USA, for monkeys). Serum CX3CL1 levels were measured by an ELISA kit (Mouse Fractalkine (CX3CL1) ELISA Kit, Cat. ab100683, ABCAM, UK). As for glucose tolerance test (GTT), the mice were fasted and water deprived for 12 h, and then received intraperitoneal injection with 2 g of glucose/kg body weight (Glucose monohydrate, Cat. 10010518, HUSHI, China). Blood glucose levels were measured prior to treatments with various agents and after treatments at 15, 30, 60, 90, and 120 minutes. For insulin tolerance test (ITT), mice fed with vehicle-, 15% sucrose- or 0.15% APM-HFCD were treated with similar protocols described for GTT measurements, except receiving intraperitoneal injection of insulin (0.5 U/kg body weight, Novolin 30R, Cat. 8-0267-03-260-1, Novo Nordisk, Denmark). Blood glucose levels were measured prior to treatments and at time points at 15-, 30-, and 60-min post injection.

Oil Red O staining of mouse aortas

Freshly isolated aortas from ApoE$^{-/-}$ mice were dissected longitudinally along the vessels to separate the lesser curvature of arches. The aorta adventitia was carefully removed and the isolated aortas were incubated in 60% isopropanol for 10 min followed by a 2-h incubation with Oil Red O (Cat. G1015, Servicebio, China). The stained aortas were then washed with 60% isopropanol for 3 min and stored in PBS for further analysis.

Please cite this article in press as: Wu et al., Sweetener aspartame aggravates atherosclerosis through insulin-triggered inflammation, Cell Metabolism (2025), https://doi.org/10.1016/j.cmet.2025.01.006

Endothelial cell culture and treatment

An endothelial cell specific culture medium (Cat. CM-M075, Procell, China) and Matrigel (Cat. 356230, Coning, USA) were mixed in a 1:1 ratio, which were used to coat 6-well plates. The thoracic aorta was dissected from each of the 4-week-old wild-type male C57BL/6J mice under anesthetic condition. The adventitia of each thoracic aorta was separated and the exposed aorta was cut into pieces approximately 1 mm^3 in size. These small aorta pieces were carefully placed to ensure that the luminal side facing to the Matrigel-coated plates. These aorta-containing plates were cultured for 4 consecutive days, and cell migration was examined daily under a light microscope. At the time of a sufficient number of vessel wall cells migrated away from aortas, the original aorta tissue was removed from each culture well and cells were further incubated for additional 48 h. To identify the aorta-derived cells, CD31, an endothelial cell specific marker, was deployed for staining. In our experimental settings, nearly 99% of migrated cells exhibited $CD31^+$ signals, identifying them as PAECs. Cells were cultured at 37°C in a humidified atmosphere with 5% CO_2. Prior to insulin stimulation, PAECs were starved for 12 h in a serum-free endothelial cells culture medium. After 12 h starvation, insulin was added to a final concentration of 0.8 μg/mL. An identical vehicle buffer without insulin was used as a control. Stimulation with insulin at 6 h and 8 h was set for RNA and protein extraction timepoints, respectively.

H&E, Oil Red O, and Sirius red staining

Cryo-tissue sections in 5-μm thickness were incubated at 25°C for approximately 3 h. After incubation, tissue slides were incubated for 10 min in a phosphate buffered saline (Cat. 10010023, PBS, Thermo Fisher, USA). For hematoxylin and eosin (H&E) staining, the hydrated slides were stained with H&E according to the manufacturer's standard protocol (a Hematoxylin-Eosin Stain Kit, Cat. G1120, Solarbio, China). For detection of lipid droplets, tissue slides were stained at room temperature for 15 min with Oil Red O (Cat. G1015, Servicebio, China), followed by rinsed twice with 60% isopropanol for 4 seconds each time. The stained tissue slides were finally washed with distilled water. For detection of collagen I, tissue slides were stained for 30 min at room temperature with a Sirius red staining solution (Cat. PH1098, Science Phygene, China), followed by rinsing once for 4 s with distilled water.

Immunofluorescence

For immunofluorescent staining, cryo-tissue slides were incubated for 10 min in a quick antigen retrieval solution for frozen tissues (Cat. P0090, Beyotime, China) and were subsequently blocked with 4% goat serum (Cat. GK500710, Gene Tech, China). Detection of the smooth muscle-positive singles were performed at 4°C overnight using a rabbit anti-mouse α-SMA (Cat. 19245, Cell Signaling, USA, 1:200 dilution), followed by further staining at 37°C for 1 h with an Alexa Fluor 594-labeled goat anti-rabbit secondary antibody (1:200, Cat.ZF-0516, ZSGB-BIO, China). A primary rat anti-mouse MOMA-2 (Cat. ab33451, ABCAM, UK, 1:50 dilution) antibody was incubated with tissue slides to detect macrophages. Tissue sections were stained at 4°C overnight with the anti-MOMA-2, followed by staining at 37°C for 1 h with an FITC-labeled goat anti-rat secondary antibody (Cat. ZF-0315, ZSGB-BIO, China, 1:200). After incubation with secondary antibodies tissue slides were washed in a darkroom with 3× PBS for 5 min/each. The stained slides were mounted with a mounting medium containing DAPI (Cat. ab104139, ABCAM, UK).

Calculation of instability index

The plaque instability index was calculated according to the following formula: (Oil Red O^+ area plus MOMA-2^+ area) / (α-SMA^+ area plus collagen I^+ area).

Microarray analysis

Mouse PAECs in monolayers were stimulated for 8 h with 0.8 μg/mL insulin (Cat. I9278, Sigma, Germany). Saline-simulated PAECs were served as a control. Triplicate samples in each group were included in each experiment. After stimulation, total amounts of RNAs were extracted using an RNA extraction buffer (Trizol, Cat. 01761/40523, CWbio, USA). RNA concentration and quality were determined by the Qubit®3.0 Fluorometer (Life Technologies, USA) and the Nanodrop One spectrophotometer (Thermo Fisher Scientific Inc, USA), respectively. Paired-end libraries were created by using the Stranded mRNA-seq Lib Prep Kit for Illumina (ABclonal, China). The data were processed using high-throughput sequencing, and plot GO plots were generated using the ggplot algorithms. The library construction and sequencing were performed by Sinotech Genomics Co., Ltd. (Shanghai, China)

Real-time PCR

Total RNA was extracted from mouse PAECs using a Fastagen RNAfast200 kit (Cat. 220011, Fastagen, China). cDNA was synthesized using a HiScript III RT SuperMix for qPCR (Cat. R323-01, Vazyme, China). Quantitative PCR (qPCR) was performed using the ChamQ Universal SYBR qPCR Master Mix (Cat. Q711, Vazyme, China) on Light Cycler 480 instrument (Roche, Switzerland). Each qPCR reaction was performed for 35 cycles. The $2^{-\Delta\Delta CT}$ method was used to assess relative mRNA expression levels. Paired qPCR primers are shown in Table S1.

Western blot analysis

Total proteins from the insulin- and vehicle- treated PAECs were separated by a 10% SDS-PAGE (Cat. 1610183, Bio-rad, USA) and transferred onto a 0.22-μm PVDF membrane (Cat. ISEQ00010, Millipore, USA), which was blocked with 5% skim milk and further incubated at 4°C overnight with a rabbit anti-mouse CX3CL1 antibody (Cat. YT5354, Immunoway, USA). The membrane was hybridized with a horseradish-labeled goat anti-rabbit antibody (Cat. ZB-2301, ZSGB-BIO, China). Transferred blots were developed with a

chemiluminescent reagent M5 HiPer ECL Western HRP Substrate (Cat. MF074-05, Mei5 Biotech, China). The same western blot procedure was used to detect CX3CR1 protein expression in monocytes and macrophages, except a rabbit anti-mouse CX3CR1 primary antibody (Cat. ab308613, ABCAM, UK) was used.

FACS analysis

Freshly isolated mouse aorta tissues were treated at 37°C for 25 min with a mixture of 2 mg/mL type I collagenase (Cat. LS004194, Worthington, USA) and 20 mg/mL type II collagenase (Cat. LS004174, Worthington, USA), followed by filtration through a 70-μm cell strainer. The tissue lysates were centrifuged at room temperature at a rotation speed of 1000 rpm for 10 min. Cell pellets were resuspended with a FACS buffer containing 1 μg/100 μL CD16/32 (Cat. 101319, Biolegend, USA) and were further centrifuged at 1000 rpm for 10 min. Cell pellets were suspended to a final concentration 1×10^6 /mL and incubated at room temperature for 1 h with a rabbit anti-mouse CX3CL1 APC-conjugated monoclonal antibody at a final concentration corresponding to 1×10^6 cells/10 μL antibody (Cat. FAB571A, RnD system, USA). These single-cell samples were co-stained with a rat anti-mouse PE-conjugated CD31 antibody (Cat. 12-0311-82, Invitrogen, USA) and a rat anti-mouse FITC-conjugated CD45 antibody (Cat. 11-0451-82, Invitrogen, USA). Stained cells were collected by centrifugation at 1000 rpm for 10 min, followed by washing twice in PBS. Positive and negative signals were analyzed using the Beckman CytoFLEX FCM (Beckman Coulter, USA). Collected data was analyzed using a Change FlowJo 10.8.1 software.

Migration assay

RAW 264.7 monocytes (Cat. iCell-m047, ICell Bioscience Inc, China) were seeded at a density of 4.0×10^5/mL in 200 μL of DMEM medium and added to each of the upper chamber of transwells (Cat. 3422, Corning, USA). A recombinant CX3CL1 protein (Cat. 50917-M08Y, Sino Biological, China) was added to each lower chamber to make a final concentration of 5 ng/mL or 50 ng/mL in a total volume of 600 μL /well. The same volume of DMEM medium without CX3CL1 served as a negative control. After incubation for 48 h, migrating cells through the beneath side of transwells were fixed for 15 min with 4% paraformaldehyde. Migrated cells were washed with PBS and stained with crystal violet for 40 min (Cat. KGA229, KeyGEN, USA). Migrated cells were examined under a 20.0× magnification and 5 randomized fields were recorded for each biological sample. Migrated monocytes were quantified by an Image J software and average cell numbers were presented.

Cell adhesion assay

Monolayers of PAECs were cultured in parallel-plate flow chambers (Cat. 80176, ibidi, Germany). PAECs were cultured for 8 h in an endothelial cell specific culture medium (Cat. CM-M075, Procell, China), which contained 0.8 μg/mL insulin (Cat. I9278, Sigma, Germany). RAW 264.7 monocytes transduced with shRNA-expressing lentivirus (SyngenTech, China) were treated for 1 h with 0.3 mM Calcein AM (Cat. C2012, Beyotime, China). Cells were resuspended to make a final concentration of 3.0×10^6 /mL. These cells were loaded into a PAECs-coated parallel-plate flow chamber with flow rate that could create 10 dyn/cm^2 shear stress. After 2 min, the chamber was washed with a monocyte-free medium for additional 2 min. The trapped monocytes by PAECs were examined under fluorescence microscope and quantified by an Image J software, and the average cell numbers were presented.

Scanning and transmission electron microscopy

After feeding with APM- and vehicle-HFCD for 2 weeks, the arch fragments of the aortas from each ApoE$^{-/-}$ mouse were surgically dissected and fixed in 2.5% glutaraldehyde (Cat. SL1770, Coolaber, China) for 2 h. These aorta fragments were cut along the longitudinal direction of each vessel and flattened to allow the luminal side to face upwards. These aorta tissues were washed with PBS for 15 min/time for 3 times, followed by fixing in 1% osmic acid (Cat. 18456, Ted Pella Inc, USA) in a dark environment for 2 h. The fixed aortas were washed 3 times with PBS and were sequentially dehydrated 15 min in 30%-50%-70%-80%-90%-95%-100%-100% ethanol solutions. Isoamyl acetate (Sinopharm Chemical Reagent Co., Ltd. Cat. 10003128, China) was used to dehydrate these tissue samples. Dehydrated tissues were dried by Critical Point Dryers (Cat. K850, Quorum, UK). Tissue samples were placed onto a double-sided carbon tape and sprayed for 30 s with gold particles by an ion sputter coater (Cat. MC1000, HITACHI, Japan). The luminal side of the lesser curvature of the arch aorta was scanned by a scanning electron microscope (Model. SU8100, HITACHI, Japan). For analysis with transmission microscopy, the aorta tissues were sequentially dehydrated with ethanol as indicated above for 20 min each round, followed by incubation twice for 15 min/each in acetone. The tissues were sequentially penetrated by pure Epon812 (Cat. 90529-77-4, SPI, USA) at 37°C for 5-8 h. Then the issues were immersed in this solution and dried overnight at 37°C in a baker followed by further incubation in 65°C for 48 h. The tissues were longitudinally cut into 60-80 nm in thickness slides and the lesser curvature section was scanned by a transmission electron microscope (Model. HT7800, HITACHI, Japan).

Isolation of blood mononuclear cells

Blood samples from anesthetized mice were collected into anticoagulant-treated tubes and peripheral blood mononuclear cells (PBMCs) were prepared by a centrifugation method using HISTOPAQUE (Cat. 10771, Sigma-Aldrich, USA). After centrifugation, the PBMC layers were carefully harvested by a Pasteur pipette. The collected cells were further purified using a PBS solution, followed by centrifugation (250×g, 4°C, 10 min). Contaminant red blood cells (RBCs) were lysed using an RBC lysis buffer (Cat. 130-094-183, Miltenyi, Germany). After termination of RBC lysis with 2% FBS, purified PBMCs were collected by centrifugation and frozen cells were used for single-cell RNA sequencing (scRNAseq) analysis.

Please cite this article in press as: Wu et al., Sweetener aspartame aggravates atherosclerosis through insulin-triggered inflammation, Cell Metabolism (2025), https://doi.org/10.1016/j.cmet.2025.01.006

Single cell-RNA sequencing

PBMCs from Cx3cr1$^{flox/flox}$ and Cx3cr1$^{M\Phi-/-}$ mice were analyzed using 10× Genomics. Raw gene expression matrices of each sample were generated using the Cell Ranger (v6.1.2) pipeline coupled with the mouse reference version GRCh38 (n = 3 samples/group). Outputs of filtered gene expression matrices were analyzed by a R software (version 4.3.1) with the Seurat package (version 4.4.0).[48] Cells were further filtered before dimensionality reduction (nFeature_RNA-min. 200; nFeature_RNA-max. 3000; percent.mt-max. 10%) (Table S2). An scDblFinder method of scDblFinder[49] (v1.16.0) R package was used to identify and remove potential doublets. Expression values were scaled to 10,000 transcripts per cells and Log-transformed (NormalizeData function, normalization.method = ''LogNormalize'', scale.factor = 10000). We calculated variable features by the FindVariableFeatures function using selection.method="vst" and nfeatures = 2000. RunPCA function was analyzed using default parameters on linear-transformation scaled data generated by the ScaleData function to reduce dimensionality of the dataset. Then the ElbowPlot functions were used to identify proper dimensions of the dataset (first 14 PCs).

To identify cell clusters, we performed the FindNeighbors function prior to clustering, which was referred as an input of the previously defined dimensionality of datasets (first 14 PCs). Clustering was performed using the FindClusters function at a value of 0.3 for the resolution parameter. After non-linear dimensional reduction and projection of all cells into two-dimensional space by UMAP, clusters were assigned preliminary identities based on the expression of combinations of known marker genes for major cell classes and types.

Differential expression of genes

Differential gene expression testing was performed using the FindAllMarkers function in Seurat with parameter only.pos = TRUE. Differential expression genes (DEGs) were filtered using a maximal p value of 0.05. Dot plots showed the relative average expression of the top 5 DEGs in each of subclusters. Additionally, sub-clustering was performed on myeloid cells to reduce other cell types and subtypes. Sub-clustering was performed by a standard workflow, which was similar as before with a different dimensionality (first 15 PCs) and a value of 0.9 for the resolution parameter. We selected DEGs with $p < 0.05$, avg_log2FC > 0.25 and pct.1 > 0.2 to perform enrichment analyses. The enrichment analysis was conducted by the clusterProfiler version 4.10.0 R package.[50] GO gene set (GO:0050728, GO:0050729) enrichment analysis was applied to gene set enrichment analysis (GSEA) function provided by clusterProfiler (version 4.10.0) package.

Inflammatory score assessments

To evaluate the functional variations among the monocyte/macrophage subtypes, we calculated inflammatory scores for each cell subtype based on the two GO terms (GO:0050728, GO:0050729). Each score was calculated by the AddModuleScore function of Seurat package and gsva function of the GSVA (v1.50.1) R package.[51]

Pseudotime analysis by Monocle

Trajectory inference was performed using Monocle version 2.30.0 with parameters as recommended by the developers (Analytical Biosciences Limited, Beijing, China).[52] Raw count data from the Seurat object was converted to a CellDataSet object using the newCellDataSet function in monocle, followed by the differentialGeneTest (cutoff of $q < 0.01$) function to identify variable genes. The top 5000 significant genes were ordered by the setOrderingFilter function. The reduceDimension function (reduction_method = ''DDRTree'') was used to reduce the space down to one with two dimensions. The visualization function plot_cell_trajectory was used in the ordered cells to plot each group along the same pseudotime trajectory.

QUANTIFICATION AND STATISTICAL ANALYSIS

All data are presented as the mean ± SEM using the GraphPad Prism v8.2.1.441 software for visualization. In all experiments, we minimized bias by randomizing the order of examination. Data analysis was performed using independent-samples t-test for two groups, one-way ANOVA for more than two groups, and repeated measures ANOVA for experiments with repeated measures of time. If the repeated measures ANOVA shows a statistically significant interaction between intervention and time, post-hoc analysis (Bonferroni) will be conducted to compare differences among intervention groups at each time point. All statistical analyses were performed using the IBM SPSS Statistics 26 version. Statistical details of experiments can be found in each of their corresponding figure legends. $p < 0.05$ was deemed statistically significant; $p < 0.01$ was deemed very significant; $p < 0.001$ was deemed extremely significant.